Bayesian Seismic AVO Inversion Using a Laterally Coupled Multimodal Prior Model

Ole Bernhard Forberg, Øyvind Kjøsnes, and Henning Omre

***Abstract*— A Bayesian seismic amplitude versus offset (AVO) inversion scheme with a laterally coupled prior model for porosity, water saturation, and volume of clay is proposed. A 2-D section and a 3-D volume of an oil reservoir are studied. The oil reservoir is considered at the initial state, which entails gravitationally induced bimodality in the water saturations along vertical traces. A selection Gaussian random field (S-GRF) prior model, capable of representing this bimodality, is specified for porosity, water saturation, and volume of clay. The S-GRF is specified to have lateral correlation, which may reduce the impact of trace-unique signal errors in the seismic AVO data on the inversion results. The likelihood model is linear and Gaussian, for which the S-GRF prior model is conjugate; hence, the posterior model is also an S-GRF. The form of the posterior distribution is therefore known and its parameter values can be analytically computed. Real seismic AVO data from the 2-D section and the 3-D volume are inverted and the results appear to be reliable along validation wells and represent a geologically plausible reservoir design. Furthermore, a notable variance reduction in the laterally coupled posterior model relative to an alternative posterior model without lateral coupling is achieved.**

***Index Terms*— Bayes methods, geophysics, inverse problems, mathematical model, reservoirs, rocks, statistics.**

I. Introduction

THE seismic properties of a reservoir are related to its petrophysical properties, which are the basis for reservoir characterization. Porosity and water saturation are informative about the storage capacity and fluid content of a reservoir and may adequately characterize reservoirs that have a relatively homogeneous lithology. Within a fixed lithotype, the seismic velocities and density tend to be negatively correlated with porosity, and the seismic velocities are higher in pores filled with water than in pores filled with hydrocarbon [19]. However, lithological heterogeneity may induce effects in the seismic properties that cannot be accounted for by porosity and water saturation alone; hence, a lithological variable may be necessary to adequately characterize such reservoirs [12], [24]. Seismic amplitude versus offset (AVO) data are often collected in order to characterize reservoirs. These data can be related to petrophysical properties by seismic models based on the Zoeppritz equations [28] and rock physics models. A seismic model can either be approximated or be based on full waveform, and similarly, a rock physics model can either be approximated from empirical data or be based on poroelasticity theory [19].

In practice, the seismic AVO data are known, while the petrophysical properties are unknown. The prediction of the petrophysical properties from the seismic AVO data can be formulated as an inverse problem [26]. Seismic inverse problems are often approached probabilistically, in a Bayesian framework [5], [14], [18]. This framework requires the definition of a likelihood model and a prior model, which together determine the form of the solution [27]. The likelihood model is a probabilistic forward model describing the data acquisition procedure and is often comprised of an approximate forward function and a stochastic error term [5], [10], [13]. The prior model is a probability distribution representing knowledge and beliefs about the properties to be predicted. The Bayesian solution to the inverse problem is the posterior model, which is a probability distribution proportional to the product of the likelihood model and the prior model. A Gauss-linear likelihood model, defined by a linear forward model with Gaussian error terms, paired with a Gaussian random field (GRF) prior model, yields a computationally advantageous solution in a Bayesian seismic inversion framework [6]. These model assumptions are convenient because Gaussian prior models are conjugate with respect to Gauss-linear likelihood models, i.e., the posterior model is of the same form as the prior model. Consequently, the posterior model is Gaussian, which is extremely computationally advantageous in high-dimensional settings since predictive quantities can be analytically computed. Should these Gaussian assumptions be unjustifiable, one may use Markov chain Monte Carlo (McMC) methods [4], [8], [20], [22], [25] to assess the posterior distribution. These techniques are based on iterative algorithms that usually obtain samples from the posterior model by generating proposals from the prior model that are accepted or rejected based on the Metropolis rule applied to the likelihood of the proposed and current sample. McMC algorithms tend to converge slowly for models that are defined on large spatial grids with strong spatial coupling; hence, the approach may be problematic in such cases.

Porosity and water saturation, and other continuous petrophysical or elastic properties, seldom appear as Gaussian due to underlying lithology and fluid classes. Rather, they appear as multimodal [12]; hence, a Gaussian prior model is usually not appropriate. A mixture Gaussian model [15] offers support for multimodality and can be used in spatial settings. A spatial definition of the mixture Gaussian model requires a spatially defined mode indicator, for which a Markov random

Manuscript received April 16, 2021; revised August 4, 2021; accepted September 4, 2021. This work was supported by the Uncertainty in Reservoir Evaluation (URE) Research Activity at Norwegian University of Science and Technology (NTNU). *(Corresponding author: Ole Bernhard Forberg.)*

Ole Bernhard Forberg and Henning Omre are with the Department of Mathematical Sciences, Norwegian University of Science and Technology, 7491 Trondheim, Norway (e-mail: ole.b.forberg@ntnu.no).

Øyvind Kjøsnes is with Aker BP, 7011 Trondheim, Norway.

Digital Object Identifier 10.1109/TGRS.2021.3113865

field prior model has been proposed [9], [24]. An advantage of this approach is that the mixture Gaussian model is a conjugate prior model with respect to Gauss-linear likelihood models. However, evaluation of the posterior distribution is computationally demanding and relies on McMC algorithms. An alternative approach relies on a selection Gaussian random field (S-GRF) prior model. The concept of selection probability distributions [3] has been developed and extended to spatial settings [2], [21] and has been applied to seismic inversion [10], [16], [23]. This approach is further explored in the current study.

We extend the study in [10] to invert a 2-D section and a 3-D volume of a reservoir and use data from the same oil and gas discovery in the North Sea. However, whereas porosity and water saturation could provide adequate reservoir characterization in [10], the chosen inversion zones in the current study are more lithologically heterogeneous and contain a mix of sand and shale. Therefore, we are also interested in characterizing the clay content in the inversion zones. We operate in a Bayesian framework. The forward model consists of an empirically approximated rock physics model combined with the linearized seismic AVO formulation used in [5]. The seismic model is a wavelet convolution of the linear Aki and Richards [1] approximation of the Zoeppritz equations [28]. From this model, the seismic AVO responses are predicted from the elastic properties: P-wave velocity, S-wave velocity, and density. The rock physics model is approximated by multiple linear regressions of the logarithmic elastic properties on porosity, water saturation, and volume of clay [10], [13], [17]. We associate Gaussian error terms with the forward function; hence, the likelihood model is Gauss-linear. The prior model is an S-GRF, which provides support for multimodality and is conjugate with respect to the Gauss-linear likelihood model [21]. Moreover, the S-GRF prior model is laterally coupled with support for volume of clay. To facilitate the extensions made in the current study, a feasible sampling scheme for higher dimensions, which honors lateral coupling and supports different anisotropy for porosity and water saturation, is developed. The methodology is demonstrated on real 2-D and 3-D data from the Kneler field in the Alvheim oil and gas field in the North Sea.

II. Definitions and Notation

The reservoir zone under study is of spatial dimension m and it is discretized into the reservoir grid $\mathcal{G}_r$, consisting of n_r grid points. The petrophysical properties of interest in the reservoir zone are referred to as reservoir properties. In the current study, the reservoir properties are porosity, water saturation, and volume of clay, which are contained in the n_r-dimensional vectors $\boldsymbol{\phi}$, $\mathbf{s}_\mathrm{w}$, and $\mathbf{v}_\mathrm{c}$, respectively. Hence, the reservoir properties are represented by the $3n_r$-dimensional vector $\mathbf{r} = [\boldsymbol{\phi}, \mathbf{s}_\mathrm{w}, \mathbf{v}_\mathrm{c}]$. The following shorthand notation is useful:

$$\mathbf{r}_k = \begin{cases} \boldsymbol{\phi}, & \text{for } k = 1 \\ \mathbf{s}_\mathrm{w}, & \text{for } k = 2 \\ \mathbf{v}_\mathrm{c}, & \text{for } k = 3. \end{cases} \tag{1}$$

Seismic AVO data informative about the reservoir properties are available on the seismic grid $\mathcal{G}_d$, consisting of n_d grid points. These data are represented by the $n_\theta n_d$-dimensional vector $\mathbf{d}$, where n_θ is the number of offset angles. The elastic properties on logarithmic form are contained in the $3n_r$-dimensional vector $\mathbf{m} = [\log(\mathbf{v}_\mathrm{p}), \log(\mathbf{v}_\mathrm{s}), \log(\boldsymbol{\rho})]$, where the three n_r-dimensional vectors $\mathbf{v}_\mathrm{p}$, $\mathbf{v}_\mathrm{s}$, and $\boldsymbol{\rho}$ contain the P-wave velocities, S-wave velocities, and densities, respectively. All vectors, defined and yet to be defined, are column vectors unless otherwise stated. An $(n_1 \times n_2)$ matrix is a matrix with n_1 rows and n_2 columns, and $\mathbf{I}_n$ is the $(n \times n)$ identity matrix. The superscript T indicates the transpose.

The reservoir properties are assumed to be stochastic; hence, $\mathbf{r}$ is a random vector, implying the existence of an associated probability density function (pdf) and a corresponding cumulative density function (cdf), denoted by $p(\mathbf{r})$ and $P(\mathbf{r})$, respectively. Moreover, since each element of $\mathbf{r}$ is considered to be a random variable associated with a specific location in the reservoir grid $\mathcal{G}_r$, $\mathbf{r}$ is a so-called discretized random field (RF).

The RF $\mathbf{r}$ is a discretized GRF if its pdf is Gaussian, i.e., of the form

$$p(\mathbf{r}) = (2\pi)^{-\frac{3n_r}{2}} |\boldsymbol{\Sigma}_r|^{-\frac{1}{2}} \exp\left\{ -\frac{1}{2} (\mathbf{r} - \boldsymbol{\mu}_r)^T \boldsymbol{\Sigma}_r^{-1} (\mathbf{r} - \boldsymbol{\mu}_r) \right\} \tag{2}$$

where $\boldsymbol{\mu}_r$ is the $3n_r$-dimensional expectation vector and $\boldsymbol{\Sigma}_r$ is the $(3n_r \times 3n_r)$ covariance matrix. This pdf is denoted by $\varphi_{3n_r}(\mathbf{r}; \boldsymbol{\mu}_r, \boldsymbol{\Sigma}_r)$. The probability that $\mathbf{r}$ belongs to a subset $\mathbf{Q}$ of the $3n_r$-dimensional space of real numbers is denoted by $\Phi_{3n_r}(\mathbf{Q}; \boldsymbol{\mu}_r, \boldsymbol{\Sigma}_r)$ and given by the integral

$$\begin{aligned} \Phi_{3n_r}(\mathbf{Q}; \boldsymbol{\mu}_r, \boldsymbol{\Sigma}_r) &= \mathrm{Prob}(\mathbf{r} \in \mathbf{Q}) \\ &= \int_{\mathbb{R}^{3n_r}} I(\mathbf{r} \in \mathbf{Q}) \varphi_{3n_r}(\mathbf{r}; \boldsymbol{\mu}_r, \boldsymbol{\Sigma}_r)\, \mathrm{d}\mathbf{r} \end{aligned} \tag{3}$$

where $I(\cdot)$ is the indicator function, which is equal to 1 if the argument is true and equal to 0 otherwise.

The RF $\mathbf{r}$ is a discretized S-GRF if its pdf is selection Gaussian, i.e., of the form demonstrated in [3], [21]

$$\begin{aligned} p(\mathbf{r}) = p(\tilde{\mathbf{r}} | \boldsymbol{\nu} \in \mathbf{A}) &= \frac{p(\boldsymbol{\nu} \in \mathbf{A} | \tilde{\mathbf{r}})}{p(\boldsymbol{\nu} \in \mathbf{A})} p(\tilde{\mathbf{r}}) \\ &= \frac{\Phi_{n_\nu}\left(\mathbf{A}; \boldsymbol{\mu}_{\nu|\tilde{r}}, \boldsymbol{\Sigma}_{\nu|\tilde{r}}\right) \varphi_{3n_r}(\tilde{\mathbf{r}}; \boldsymbol{\mu}_{\tilde{r}}, \boldsymbol{\Sigma}_{\tilde{r}})}{\Phi_{n_\nu}\left(\mathbf{A}; \boldsymbol{\mu}_\nu, \boldsymbol{\Sigma}_\nu\right)} \end{aligned} \tag{4}$$

where $\tilde{\mathbf{r}}$ is the $3n_r$-dimensional basis variable, $\boldsymbol{\nu}$ is the n_ν-dimensional auxiliary variable, and $\mathbf{A}$ is the n_ν-dimensional selection set (see [10] for details). The conditional parameters involved in the pdf can be computed as

$$\begin{aligned} \boldsymbol{\mu}_{\nu|\tilde{r}} &= \boldsymbol{\mu}_\nu + \boldsymbol{\Gamma}_{\tilde{r}\nu} \boldsymbol{\Sigma}_{\tilde{r}}^{-1} (\tilde{\mathbf{r}} - \boldsymbol{\mu}_{\tilde{r}}) \\ \boldsymbol{\Sigma}_{\nu|\tilde{r}} &= \boldsymbol{\Sigma}_\nu - \boldsymbol{\Gamma}_{\tilde{r}\nu} \boldsymbol{\Sigma}_{\tilde{r}}^{-1} \boldsymbol{\Gamma}_{\nu\tilde{r}} \end{aligned} \tag{5}$$

where the $(3n_r \times n_\nu)$ matrix $\boldsymbol{\Gamma}_{\tilde{r}\nu}$ contains the covariances between $\tilde{\mathbf{r}}$ and $\boldsymbol{\nu}$.

The RF $\mathbf{r}$ is said to be stationary if the pdf of any subset of random variables in $\mathbf{r}$ is shift invariant; hence, the pdf must depend only on the distances between the selected random variables in the reservoir grid and not on their specific

locations. For the GRF $\mathbf{r}$, this holds if the locationwise expectations and variances are constant, and the correlation structure is spatially shift-invariant. This entails that the expectation vector and covariance matrix has the following form:

$$\boldsymbol{\mu}_{r_k} = \mu_{r_k}\mathbf{i}_{n_r}, \quad \text{and } \boldsymbol{\Sigma}_{r_k} = \sigma_{r_k}^2\boldsymbol{\Omega}_{r_k}; \quad k = 1, 2, 3 \tag{6}$$

where μ_{r_k} and $\sigma_{r_k}^2$ are the locationwise expectation and variance, respectively, and $\boldsymbol{\Omega}_{r_k}$ is the spatial correlation matrix. This spatial correlation matrix is defined through the shift-invariant and positive-definite correlation function $\rho_{r_k}(\boldsymbol{\tau})$, where $\boldsymbol{\tau}$ is the distance between two grid points. Finally, $\mathbf{i}_{n_r}$ is the n_r-dimensional vector of ones. The S-GRF $\mathbf{r}$ is said to be stationary if the criteria for a stationary GRF hold and the selection set $\mathbf{A}$ is identical in all locations, that is, if it can be expressed as the Cartesian product $\mathbf{A} = A^{n_v}$, with A a subset of the real numbers.

III. Methodology

The prediction of the reservoir properties $\mathbf{r}$ from the seismic AVO data $\mathbf{d}$ is approached in a Bayesian framework. The solution to the inverse problem is the posterior pdf $p(\mathbf{r}|\mathbf{d})$, defined by Bayes' rule

$$p(\mathbf{r}|\mathbf{d}) = \frac{p(\mathbf{d}|\mathbf{r})p(\mathbf{r})}{p(\mathbf{d})} \propto p(\mathbf{d}|\mathbf{r})p(\mathbf{r}) \tag{7}$$

where $p(\mathbf{d}|\mathbf{r})$ and $p(\mathbf{r})$ are the likelihood and prior models, respectively. The denominator $p(\mathbf{d})$ is the normalizing constant, which is generally hard to compute. The methodology is based on model assumptions for the likelihood and prior models that make analytical computation of $p(\mathbf{d})$ feasible.

A. Likelihood Model

The relationship between the seismic responses and the reservoir properties represents the seismic data acquisition procedure and is described by the likelihood model $p(\mathbf{d}|\mathbf{r})$. This model can be decomposed into a seismic likelihood model $p(\mathbf{d}|\mathbf{m})$ and a rock physics model $p(\mathbf{m}|\mathbf{r})$ (see [10] for details).

The seismic model relates the elastic properties to the seismic responses. In the current study, this model is based on a convolution of the linear Aki and Richards approximation [1] to the Zoeppritz equations and is of the form $[\mathbf{d}|\mathbf{m}] = \mathbf{WADm} + \mathbf{e}_{d|m} = \mathbf{W}(\mathbf{c} + \mathbf{e}_{c|m}) + \mathbf{e}_{d|c}$ [5], where the $n_\theta n_r$-dimensional vector $\mathbf{c}$ contains the computed reflectivity coefficients. The $(n_\theta n_r \times 3n_r)$ matrix $\mathbf{A}$ and the $(3n_r \times 3n_r)$ matrix $\mathbf{D}$ represent the Aki and Richards approximation, with $\mathbf{A}$ containing angle dependent coefficients and $\mathbf{D}$ being a first-order differential operator. Convolution is introduced through the $(n_\theta n_d \times n_\theta n_r)$ matrix $\mathbf{W}$, which contains discretizations of the seismic wavelet. Furthermore, the $n_\theta n_d$-dimensional vector $\mathbf{e}_{d|m}$ is an error term assumed to be Gaussian, with expectation zero and $(n_\theta n_d \times n_\theta n_d)$ covariance matrix $\boldsymbol{\Sigma}_{d|m} = \mathbf{W}\sigma_{c|m}^2\mathbf{I}_{n_\theta n_r}\mathbf{W}^T + \sigma_{d|c}^2\mathbf{I}_{n_\theta n_d}$. The variance $\sigma_{c|m}^2$ is associated with model error from the Aki and Richards approximation, while the variance $\sigma_{d|c}^2$ is associated with observation error. Note that $\mathbf{e}_{d|m}$ contains both white and colored noise since the model error is wavelet convolved. The seismic likelihood model is Gauss-linear and can be expressed as

$$p(\mathbf{d}|\mathbf{m}) = \varphi_{n_\theta n_d}\big(\mathbf{d};\, \mathbf{WADm},\, \boldsymbol{\Sigma}_{d|m}\big). \tag{8}$$

The rock physics model relates the reservoir properties to the elastic properties. As in previous studies [10], [11], the model is inspired by Landrø [17] and formulated as a multiple linear regression, $[\mathbf{m}|\mathbf{r}] = \mathbf{Br} + \mathbf{e}_{m|r}$. Regression coefficients from multiple linear regressions of the logarithmic elastic properties on the reservoir properties are contained in the $(3n_r \times 3n_r)$ matrix $\mathbf{B}$, while the $3n_r$-dimensional vector $\mathbf{e}_{m|r}$ represents the error associated with the model. The error term $\mathbf{e}_{m|r}$ is assumed to be Gaussian with expectation zero and $(3n_r \times 3n_r)$ covariance matrix $\boldsymbol{\Sigma}_{m|r}$. Hence, the rock physics likelihood model is Gauss-linear and can be expressed as

$$p(\mathbf{m}|\mathbf{r}) = \varphi_{3n_r}\big(\mathbf{m};\, \mathbf{Br},\, \boldsymbol{\Sigma}_{m|r}\big). \tag{9}$$

Alternatively, a linear rock physics model can, for example, be based on a linearized theoretical model [7]. The seismic and rock physics model applied in succession define the forward model, which takes the form $[\mathbf{d}|\mathbf{r}] = \mathbf{Gr} + \mathbf{e}_{d|r}$. Here, the $(n_\theta n_d \times 3n_r)$ matrix $\mathbf{G} = \mathbf{WADB}$ is the forward operator and the $n_\theta n_d$-dimensional vector $\mathbf{e}_{d|r} = \mathbf{WADe}_{m|r} + \mathbf{e}_{d|m}$ is an error term assumed to be Gaussian with expectation zero and $(n_\theta n_d \times n_\theta n_d)$ covariance matrix $\boldsymbol{\Sigma}_{d|r} = \mathbf{WAD}\boldsymbol{\Sigma}_{m|r}(\mathbf{WAD})^T + \boldsymbol{\Sigma}_{d|m}$. Hence, the likelihood model is Gauss-linear and can be expressed as

$$p(\mathbf{d}|\mathbf{r}) = \varphi_{n_\theta n_d}\big(\mathbf{d};\, \mathbf{Gr},\, \boldsymbol{\Sigma}_{d|r}\big). \tag{10}$$

The Gauss linearity of the likelihood model entails that for certain parametric prior models, the posterior model will be of the same form as the prior model [11].

We use the signal-to-noise ratio (SNR) as a measure of the magnitude of error in the seismic data. The SNR is defined as

$$\text{SNR} = \frac{\text{Trace}(\text{Var}(\mathbf{Gr}))}{\text{Trace}(\text{Var}(\mathbf{d}|\mathbf{r}))} = \frac{\text{Trace}\big(\mathbf{G}\boldsymbol{\Sigma}_r\mathbf{G}^T\big)}{\text{Trace}\big(\boldsymbol{\Sigma}_{d|r}\big)} \tag{11}$$

with Trace$(\cdot)$ being a function returning the sum of the diagonal elements of its matrix argument. SNR is dependent on the prior model specification because $\boldsymbol{\Sigma}_r$ is involved in the expression.

B. Prior Model

The prior model $p(\mathbf{r})$ represents our understanding, experience, and beliefs about the reservoir properties to be predicted. We operate in a setting where porosity is assumed to be predominantly spatially smoothly varying and to have a locationwise skewed and unimodal pdf. Water saturation and volume of clay are assumed to exhibit abrupt spatial transitions and to have locationwise bimodal pdfs. We base the model construction on the decomposition

$$p(\tilde{\mathbf{r}}, \boldsymbol{v}) = p(\boldsymbol{v}|\tilde{\mathbf{r}})p(\tilde{\mathbf{r}}). \tag{12}$$

The basis variable $\tilde{\mathbf{r}}$ is assumed to be a stationary GRF

$$p(\tilde{\mathbf{r}}) = \varphi_{3n_r}(\tilde{\mathbf{r}};\, \boldsymbol{\mu}_{\tilde{r}},\, \boldsymbol{\Sigma}_{\tilde{r}}) \tag{13}$$

with

$$\boldsymbol{\mu}_{\tilde{\mathbf{r}}} = \begin{bmatrix} \mu_{\tilde{\phi}}\mathbf{i}_{n_r} \\ \mu_{\tilde{s}_w}\mathbf{i}_{n_r} \\ \mu_{\tilde{v}_c}\mathbf{i}_{n_r} \end{bmatrix}$$

$$\boldsymbol{\Sigma}_{\tilde{\mathbf{r}}} = \begin{bmatrix} \sigma^2_{\tilde{\phi}}\boldsymbol{\Omega}_s & \lambda_1\sigma_{\tilde{\phi}}\sigma_{\tilde{s}_w}\boldsymbol{\Omega}_x & \lambda_2\sigma_{\tilde{\phi}}\sigma_{\tilde{v}_c}\boldsymbol{\Omega}_s \\ \lambda_1\sigma_{\tilde{\phi}}\sigma_{\tilde{s}_w}\boldsymbol{\Omega}_x & \sigma^2_{\tilde{s}_w}\boldsymbol{\Omega}_h & \lambda_3\sigma_{\tilde{s}_w}\sigma_{\tilde{v}_c}\boldsymbol{\Omega}_x \\ \lambda_2\sigma_{\tilde{\phi}}\sigma_{\tilde{v}_c}\boldsymbol{\Omega}_s & \lambda_3\sigma_{\tilde{s}_w}\sigma_{\tilde{v}_c}\boldsymbol{\Omega}_x & \sigma^2_{\tilde{v}_c}\boldsymbol{\Omega}_s \end{bmatrix}. \quad (14)$$

Here, $(\mu_{\tilde{\phi}}, \mu_{\tilde{s}_w}, \mu_{\tilde{v}_c})$ and $(\sigma^2_{\tilde{\phi}}, \sigma^2_{\tilde{s}_w}, \sigma^2_{\tilde{v}_c})$ are the locationwise expectations and variances of $\tilde{\boldsymbol{\phi}}$, $\tilde{\mathbf{s}}_w$, and $\tilde{\mathbf{v}}_c$, respectively. Moreover, $(\lambda_1, \lambda_2, \lambda_3)$ are the locationwise correlations between $\tilde{\boldsymbol{\phi}}$ and $\tilde{\mathbf{s}}_w$, between $\tilde{\boldsymbol{\phi}}$ and $\tilde{\mathbf{v}}_c$, and between $\tilde{\mathbf{s}}_w$ and $\tilde{\mathbf{v}}_c$, respectively. Finally, $(\boldsymbol{\Omega}_s, \boldsymbol{\Omega}_h, \boldsymbol{\Omega}_x)$ are $(n_r \times n_r)$ correlation matrices containing structural spatial correlation, horizontal spatial correlation, and a mix between structural and horizontal spatial correlation, respectively. Different spatial correlation structures are needed because porosity and volume of clay are defined by previous sedimentation, whereas water saturation is governed largely by current gravitation; hence, their anisotropies are likely to differ. The correlation matrices are defined through shift-invariant and positive-definite correlation functions $\rho_{r_k}(\boldsymbol{\tau}; \boldsymbol{\alpha}_k)$. The correlation structure between water saturation and the other reservoir properties is defined to be $\boldsymbol{\Omega}_x = (1/2)\boldsymbol{\Omega}_s + (1/2)\boldsymbol{\Omega}_h$.

The auxiliary GRF $\boldsymbol{\nu}$ is defined on the reservoir grid $\mathcal{G}_r$ and we define one auxiliary variable for each basis variable, i.e., $\boldsymbol{\nu} = [\boldsymbol{\nu}_1, \boldsymbol{\nu}_2, \boldsymbol{\nu}_3]$. Hence, $n_\nu = 3n_r$. The conditional relation between the auxiliary variable $\boldsymbol{\nu}$ and the basis variable $\tilde{\mathbf{r}}$ is

$$p(\boldsymbol{\nu}|\tilde{\mathbf{r}}) = \prod_{k=1}^{3} p(\boldsymbol{\nu}_k|\tilde{\mathbf{r}}_k) = \prod_{k=1}^{3} \varphi_{n_r}(\boldsymbol{\nu}_k; \boldsymbol{\mu}_{\nu_k|\tilde{r}_k}, \boldsymbol{\Sigma}_{\nu_k|\tilde{r}_k})$$
$$= \prod_{k=1}^{3}\left(\prod_{i=1}^{n_r} \varphi_1(\nu_{k,i}; \mu_{\nu_{k,i}|\tilde{r}_k}, (1-\gamma_k^2))\right). \quad (15)$$

Here, γ_k is the locationwise correlation between $\tilde{\mathbf{r}}_k$ and $\boldsymbol{\nu}_k$, and the conditional expectation is $\boldsymbol{\mu}_{\nu_k|\tilde{r}_k} = 0\mathbf{i}_{n_r} + \boldsymbol{\Gamma}_{\tilde{r}_k\nu_k}\boldsymbol{\Sigma}^{-1}_{\tilde{r}_k}(\tilde{\mathbf{r}}_k - \boldsymbol{\mu}_{\tilde{r}_k})$, $k = 1, 2, 3$. The $(n_r \times n_r)$ cross-covariance matrix $\boldsymbol{\Gamma}_{\tilde{r}_k\nu_k}$ contains the covariances between $\tilde{\mathbf{r}}_k$ and $\boldsymbol{\nu}_k$ and can be found on the diagonal of the $(3n_r \times 3n_r)$ cross-covariance matrix $\boldsymbol{\Gamma}_{\tilde{r}\nu}$

$$\boldsymbol{\Gamma}_{\tilde{r}\nu} = \begin{bmatrix} \gamma_1\sigma_{\tilde{\phi}}\boldsymbol{\Omega}_s & \lambda_1\gamma_2\sigma_{\tilde{\phi}}\boldsymbol{\Omega}_x & \lambda_2\gamma_3\sigma_{\tilde{\phi}}\boldsymbol{\Omega}_s \\ \lambda_1\gamma_1\sigma_{\tilde{s}_w}\boldsymbol{\Omega}_x & \gamma_2\sigma_{\tilde{s}_w}\boldsymbol{\Omega}_h & \lambda_3\gamma_3\sigma_{\tilde{s}_w}\boldsymbol{\Omega}_x \\ \lambda_2\gamma_1\sigma_{\tilde{v}_c}\boldsymbol{\Omega}_s & \lambda_3\gamma_2\sigma_{\tilde{v}_c}\boldsymbol{\Omega}_x & \gamma_3\sigma_{\tilde{v}_c}\boldsymbol{\Omega}_s \end{bmatrix}. \quad (16)$$

Note that the expectation $\boldsymbol{\mu}_{\nu_k|\tilde{r}_k}$ is linear in $\tilde{\mathbf{r}}$ and the conditional pdf $p(\boldsymbol{\nu}|\tilde{\mathbf{r}})$ in (15) is Gaussian; hence, the auxiliary GRF is defined to be Gauss-linearly related to the basis GRF, which entails that their joint pdf $p(\tilde{\mathbf{r}}, \boldsymbol{\nu})$ is Gaussian. Moreover, locationwise conditional independence for $[\boldsymbol{\nu}|\tilde{\mathbf{r}}]$ is assumed.

The $(3n_r \times 3n_r)$ covariance matrix associated with the auxiliary GRF $\boldsymbol{\nu}$ is

$$\boldsymbol{\Sigma}_\nu = \begin{bmatrix} \boldsymbol{\Sigma}_{\nu_1} & \lambda_1\gamma_1\gamma_2\boldsymbol{\Omega}_x & \lambda_2\gamma_1\gamma_3\boldsymbol{\Omega}_s \\ \lambda_1\gamma_1\gamma_2\boldsymbol{\Omega}_x & \boldsymbol{\Sigma}_{\nu_2} & \lambda_3\gamma_2\gamma_3\boldsymbol{\Omega}_x \\ \lambda_2\gamma_1\gamma_3\boldsymbol{\Omega}_s & \lambda_3\gamma_2\gamma_3\boldsymbol{\Omega}_x & \boldsymbol{\Sigma}_{\nu_3} \end{bmatrix} \quad (17)$$

where

$$\boldsymbol{\Sigma}_{\nu_k} = \begin{cases} \gamma_1^2\boldsymbol{\Omega}_s + (1-\gamma_1^2)\mathbf{I}_{n_r}, & k = 1 \\ \gamma_2^2\boldsymbol{\Omega}_h + (1-\gamma_2^2)\mathbf{I}_{n_r}, & k = 2 \\ \gamma_3^2\boldsymbol{\Omega}_s + (1-\gamma_3^2)\mathbf{I}_{n_r}, & k = 3. \end{cases} \quad (18)$$

Finally, the $3n_r$-dimensional selection set $\mathbf{A} = [\mathbf{A}_1, \mathbf{A}_2, \mathbf{A}_3]$ consists of the selection sets $\mathbf{A}_k$ corresponding to $\boldsymbol{\nu}_k$, $k = 1, 2, 3$. These selection sets are of the form $\mathbf{A}_k = A_k^{n_r}$, where $A_k = \bigcup_{i=1}^{n_{A_k}}[a_{k,i}, b_{k,i}]$ are subsets of the real numbers, with n_{A_k} being the number of disjoint subsets that selection set A_k consists of. The prior model for the reservoir properties, $p(\mathbf{r})$, is the trivariate discretized stationary S-GRF

$$p(\mathbf{r}) = p(\tilde{\mathbf{r}}|\boldsymbol{\nu} \in \mathbf{A})$$
$$= \frac{\prod_{k=1}^{3}\prod_{i=1}^{n_r}\varphi_1(A_k; \mu_{\nu_{k,i}|\tilde{r}_k}, (1-\gamma_k^2))}{\Phi_{3n_r}(\mathbf{A}; 0\mathbf{i}_{3n_r}, \boldsymbol{\Sigma}_\nu)}\varphi_{3n_r}(\tilde{\mathbf{r}}; \boldsymbol{\mu}_{\tilde{r}}, \boldsymbol{\Sigma}_{\tilde{r}}). \quad (19)$$

This prior model is parameterized by $\boldsymbol{\Theta}_p^{SG} = \{[\mu_{\tilde{r}_k}, \sigma^2_{\tilde{r}_k}, \lambda_k, \gamma_k, A_k, \rho_{r_k}(\cdot)]; k = 1, 2, 3\}$, where the first five parameters for each k are primarily related to the locationwise trivariate selection Gaussian pdf, whereas the last parameter for each k primarily relates to the spatial correlation structure.

The prior model $p(\mathbf{r})$ has support for values outside the physical range $[0, 1]$ of the reservoir properties. In line with [10], we correct for this effect in the predictor and prediction intervals, which is described in Section III-C.

The spatial correlation functions are for pairs of grid points defined as

$$\rho_{r_k}(\boldsymbol{\tau}; \boldsymbol{\alpha}_k) = \exp\left\{-\frac{\tau_v}{\alpha_{v,k}}\right\} \times \exp\left\{-\frac{\tau_h}{\alpha_{h,k}}\right\}; \quad k = 1, 2, 3 \quad (20)$$

where $\boldsymbol{\tau} = [\tau_v, \tau_h]$ are the grid distances, with $\tau_v \geq 0$ being the vertical distance and $\tau_h \geq 0$ being the lateral distance between the grid points. In $m = 3$ spatial dimensions, τ_h is the Cartesian distance; hence, the lateral correlation is isotropic. Finally, $\boldsymbol{\alpha}_k = [\alpha_{v,k}, \alpha_{h,k}]$ are the range parameters, being positive. These correlation functions define the spatial correlation matrices $\boldsymbol{\Omega}_s$ and $\boldsymbol{\Omega}_h$. Different anisotropies can be represented by transformation of the reservoir grid, which will be explained later.

A spatially stationary prior model may be inadequate for some applications, which is prominently exemplified by case studies that require modeling of a depth trend. A depth trend is typically modeled by a depth-dependent expectation, which can readily be accommodated by an S-GRF prior model. In a multimodal setting, a depth-dependent expectation can be defined through two mechanisms: either through a depth trend for the mode locations or through a depth trend for the mode probabilities. The former mechanism may be useful for modeling reservoir properties with a deterministic depth trend, whereas the latter mechanism can, for example, be used to model a depth-dependent belief in hydrocarbons. A depth trend for the mode locations can be achieved by defining a depth trend in $\boldsymbol{\mu}_{\tilde{r}}$. Depth-dependent mode probabilities can be defined by specifying a depth trend in $\boldsymbol{\mu}_\nu$. Alternatively, these two types of depth trends can be specified through depth-dependent selection sets.

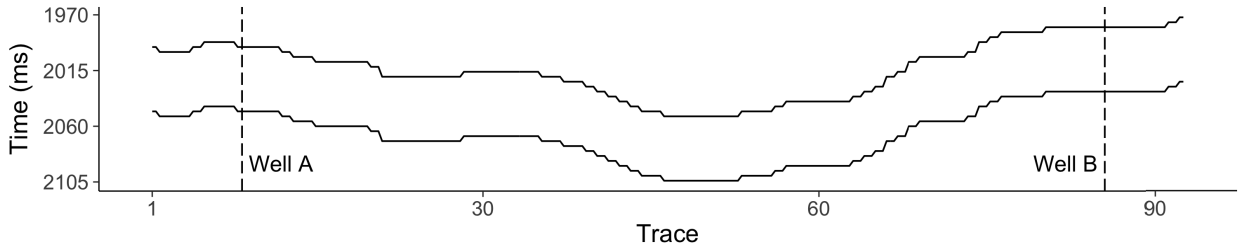

Fig. 1. Geometry of the 2-D section with wells marked.

C. Posterior Model

Because the S-GRF prior model $p(\mathbf{r})$ is conjugate with respect to the Gauss-linear likelihood model $p(\mathbf{d}|\mathbf{r})$, the posterior model $p(\mathbf{r}|\mathbf{d})$ is also an S-GRF (see [21])

$$p(\mathbf{r}|\mathbf{d}) = p(\tilde{\mathbf{r}}|\boldsymbol{\nu} \in \mathbf{A}, \mathbf{d}) = \frac{\prod_{k=1}^{3} \Phi_{n_r}\left(\mathbf{A}_k; \boldsymbol{\mu}_{\nu_k|\tilde{r}_k,d}, \boldsymbol{\Sigma}_{\nu_k|\tilde{r}_k,d}\right)}{\Phi_{3n_r}\left(\mathbf{A}; \boldsymbol{\mu}_{\nu|d}, \boldsymbol{\Sigma}_{\nu|d}\right)} \varphi_{3n_r}\left(\tilde{\mathbf{r}}; \boldsymbol{\mu}_{\tilde{r}|d}, \boldsymbol{\Sigma}_{\tilde{r}|d}\right). \tag{21}$$

The conditional parameters of this posterior model are developed in [10]. We use a block-independent Metropolis–Hastings (M-H) McMC algorithm [23] to simulate from the posterior model. These simulations form the basis for prediction and uncertainty assessment. Simulation is done either trace-by-trace or by conditioning on neighboring traces, depending on whether the lateral correlation is present or not. The McMC algorithms are presented in the Appendix.

The reservoir properties are predicted by the marginal maximum posterior (MMAP). This predictor identifies the values of the reservoir properties with the highest marginal posterior probability density at each grid point in $\mathcal{G}_r$ and is defined as

$$\hat{\mathbf{r}}_{\text{MMAP}} = \left\{ \underset{r_{k,i}}{\text{argmax}}\{p(r_{k,i}|\mathbf{d})\}; \quad k = 1, 2, 3, \ i = 1, \ldots, n_r \right\}. \tag{22}$$

Prediction intervals in the form of $(1-\alpha) \times 100\%$ highest posterior density intervals (HPDI) are used to reflect the variability in the locationwise posterior distributions [10]. These intervals may consist of a collection of disjoint regions, thereby reflecting multimodality in the posterior distribution. The MMAP is located within one of the HPDI regions. The coverage level $(1-\alpha) \times 100\%$ is user-specified and should be assigned based on considerations about the application and the shape of the distribution. Since the prior model can support nonphysical values, so can the MMAP predictions and HPDI. If they exceed $[0, 1]$, they are truncated to the appropriate limits of this range.

The MMAP prediction and accompanying $(1-\alpha) \times 100\%$ HPDI can be quantitatively evaluated if observations of the reservoir properties, $\mathbf{r}_{\text{obs}}$, are available in some locations. The root-mean-square error (RMSE) is a measure of the deviation between predictions and observations, with low values being favorable. The prediction intervals are evaluated by empirical coverage (EC), i.e., by computing the percentage of observations within the prediction intervals. EC close to the chosen coverage level of the prediction intervals is favorable.

IV. Case: Real Seismic AVO Data From a 2-D Section

We apply the proposed Bayesian seismic inversion methodology to a 2-D section of the Kneler field in the Alvheim oil and gas field, in the North Sea. The turbidite Alvheim reservoir is challenging to characterize due to complex geological depositions. The oil reservoir under study mostly consists of porous sandstone and is underlain by an aquifer, but its upper part is composed of unconsolidated and interbedded sand and shale. The chosen 2-D section, with the location of two nearby exploration wells indicated, is shown in Fig. 1. Note that the true aspect ratio of the 2-D section is altered for visualization purposes. The section has a much bigger lateral extent than what it appears to; hence, the apparent curvature in the section is much less severe. The 2-D section follows the interpreted top reservoir, ranging in depth from 1972 to 2052 ms in two-way time, for 4600 m along a cross line. Vertically, the section starts two seismic sample points above the interpreted top horizon, presumably in a top shale layer, and ends in the underlying aquifer. The 2-D section contains 93 traces with a regular inter-trace spacing of 50 m, each of which covers a depth range of 52 ms in two-way time. The reservoir grid $\mathcal{G}_r$ consists of $n_r = 2511$ grid points that are regularly spaced laterally and with trace-unique vertical gridding, whereas the seismic grid $\mathcal{G}_d$ consists of $n_d = 1302$ grid points with similar grid structure. The trace-unique vertical gridding consists of 27 points in the reservoir grid and 14 points in the seismic grid. The data and inversion results are linearly interpolated to a finer and regular grid for visualization. This artificial increase in resolution produces somewhat smoother figures, but all computations are performed on the irregular grids $\mathcal{G}_r$ and $\mathcal{G}_d$.

The exploration wells can be used for model construction and validation. Well B is in immediate vicinity of the 2-D section, whereas Well A is located a few cross lines away. Well B is the exploration well studied in [10], and its location relative to the 2-D section makes it the preferred basis for model construction. Measured well logs from Well B are shown in Fig. 2. The top reservoir is at about 1990 ms, and the underlying aquifer starts at 2020 ms, as reflected by a clear oil–water contact (OWC) in the water saturation log.

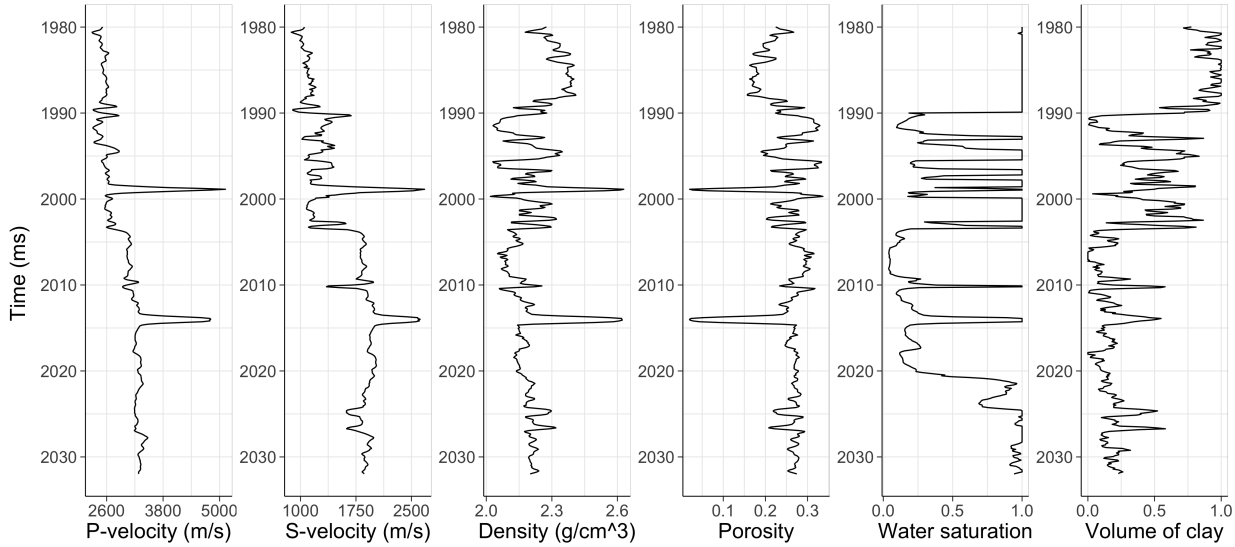

Fig. 2. Well B logs, displayed column-wise from left to right: P-wave velocity, S-wave velocity, density, porosity, water saturation, and volume of clay.

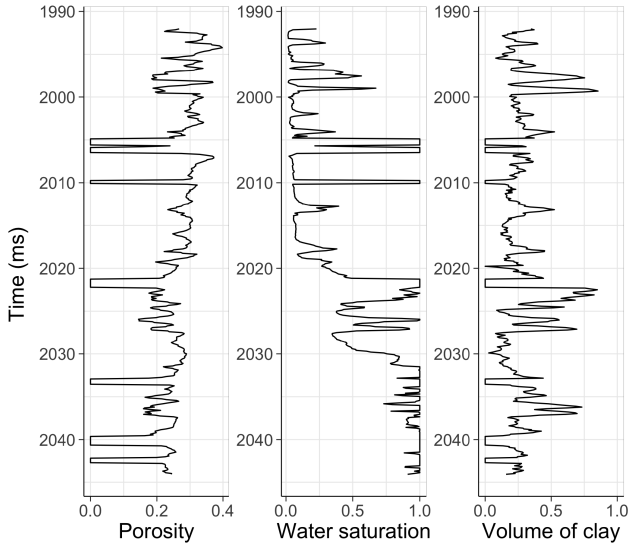

Fig. 3. Well A logs, displayed column-wise from left to right: porosity, water saturation, and volume of clay.

The characteristics of the logs above 1990 ms reflect an overlying shale layer. An increased variability in the logs can be seen between roughly 1990 and 2004 ms. This variability does not appear to be consistent with variations in the volume of clay alone; hence, there may be a notable contribution from other minerals in this region. Below 2004 ms, a more homogeneously cemented porous sandstone can be seen. Furthermore, note that the elastic properties reflect two anomalous regions, which are located at roughly 1998 and 2014 ms. These anomalies, and the above-mentioned increased variability between 1990 and 2004 ms, are likely caused by intermittently occurring limestone, which has a small presence throughout the 2-D section. Well A is used exclusively for validation of inversion results. The measured porosity, water saturation, and volume of clay along Well A are shown in Fig. 3. The oil reservoir zone appears to extend from the top of the depth interval to about 2030 ms where the underlying aquifer starts. The OWC is not as clearly reflected as in Well B since the oil–water transition seems to occur in a region that has relatively large variability in the volume of clay. Moreover, the well logs indicate specks of limestone around 2005, 2010, and 2022 ms in the oil reservoir zone.

The seismic AVO data are presented in Fig. 4, where the $n_\theta = 4$ angle stacks are displayed row-wise. The signal is relatively strong roughly between traces 20 and 35, especially in the 27° and 35° stacks, which in addition to fluid transitions may indicate a more abrupt change in lithological properties here than elsewhere. The signal in the middle part of the 2-D section, roughly between traces 40 and 65, is relatively weak in the 35° stack, indicating an absence of fluid transitions. Moreover, this region is located deeper than either side of it, which may indicate a higher content of more compressible lithologies here than elsewhere in the reservoir, for example, a higher fractional content of shale. We hereafter refer to this region as center region (CR).

A. Model Construction

Model construction entails assigning parameter values to the likelihood model $p(\mathbf{d}|\mathbf{r})$ and prior model $p(\mathbf{r})$. Because the construction is based on well logs from Well B, the model may not be adequately representative in the entire 2-D section. The effects of lateral correlation in the prior model on the inversion results are highlighted by defining an alternative prior model without lateral correlation, as in [11], for comparison. We refer to these prior models as prior models 1 and 2, corresponding to the prior model with and without lateral correlation, respectively. The inversions are carried out using SNR $= 5$.

1) Likelihood Model: The likelihood model consists of a seismic likelihood $p(\mathbf{d}|\mathbf{m})$ and a rock physics likelihood $p(\mathbf{m}|\mathbf{r})$. The matrices $\mathbf{A}$ and $\mathbf{D}$ in the seismic likelihood model are known, while the convolution matrix $\mathbf{W}$ requires estimation. The wavelet function defining $\mathbf{W}$ is chosen to be the same as in [10]; hence, the wavelet is estimated

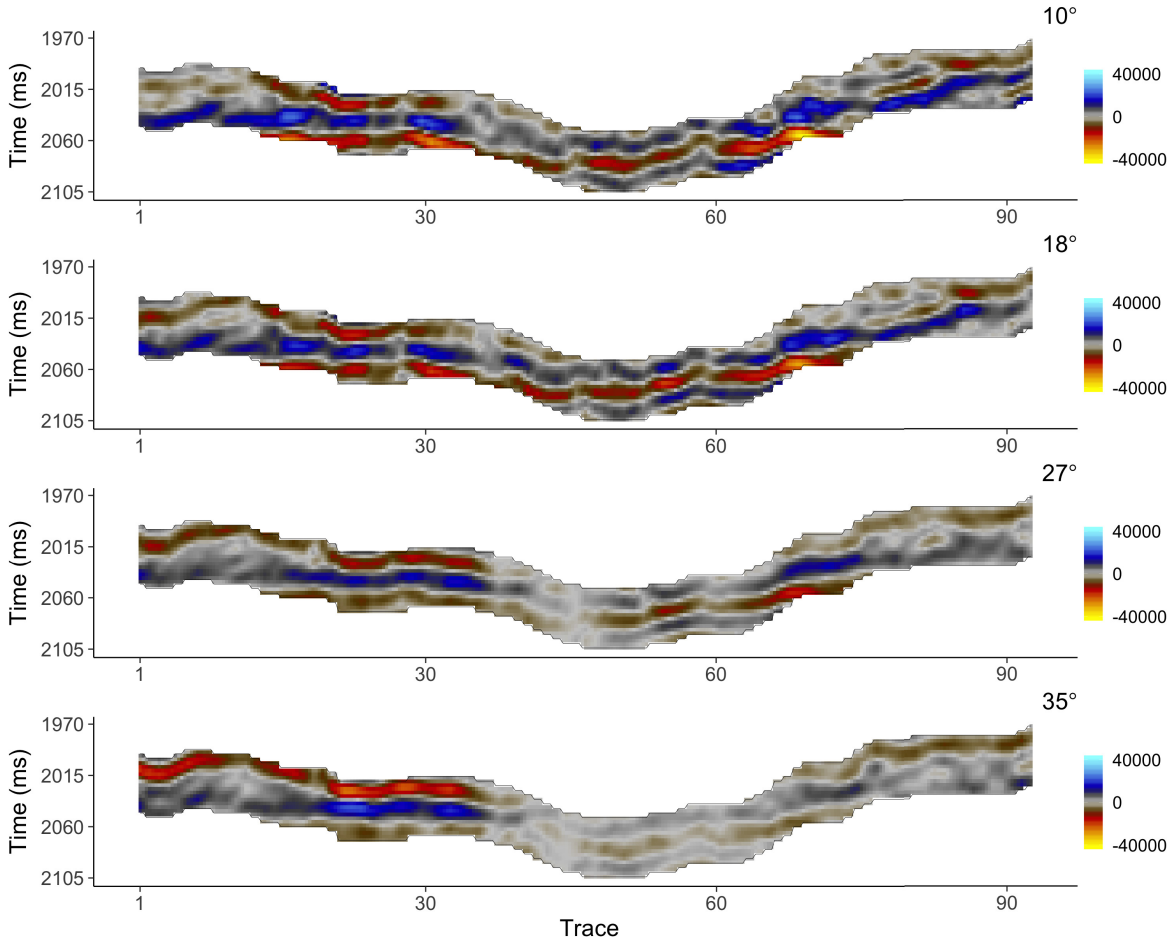

Fig. 4. Seismic AVO data from the 2-D section under study. The angle stacks 10°, 18°, 27°, and 35° are displayed in order from the top to bottom row.

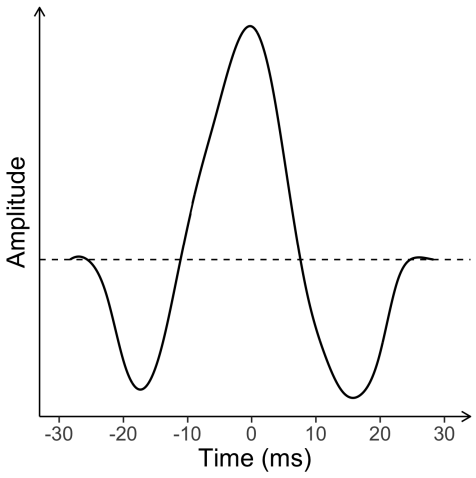

Fig. 5. Estimated wavelet.

by regressing the seismic AVO data on synthetic reflection coefficients generated from the observed elastic properties by $\mathbf{c}_{\text{mod}} = \mathbf{A}\mathbf{D}\mathbf{m}_{\text{obs}}$. The estimation is based on data from a depth interval of 300 m containing the reservoir zone and should be representative in the current study. The estimated wavelet is shown in Fig. 5.

The rock physics likelihood model requires specification of the regression matrix $\mathbf{B}$ and the covariance matrix $\Sigma_{m|r}$. The model is based on well logs from Well B after removal of the possible limestone influences. The three regression models all have an associated R^2 value of at least 0.9. In Table I, the numerical values of the estimated regression coefficients and standard deviations associated with the Gauss-linear rock physics likelihood model are displayed. Moreover, the estimated inter-covariances between the elastic properties are $(\hat{\xi}_{v_{\text{p}}v_{\text{s}}}, \hat{\xi}_{v_{\text{p}}\rho}, \hat{\xi}_{v_{\text{s}}\rho})$, with corresponding correlations (0.656, 0.319, 0.446). The performance of the rock physics model is represented graphically in Fig. 6, where the measured and rock physics predicted logarithmic elastic properties are displayed together. Note that the rock physics model performs relatively poorly in the possibly limestone-influenced interval between roughly 1990 and 2004 ms. The covariance matrix $\Sigma_{m|r}$ has the variances associated with the regressions on the diagonal and the inter-covariances $(\hat{\xi}_{v_{\text{p}}v_{\text{s}}}, \hat{\xi}_{v_{\text{p}}\rho}, \hat{\xi}_{v_{\text{s}}\rho})$ on the off-diagonal.

2) Prior Model: The parameter values used in prior model 1 are obtained by the heuristic parameter estimation approach described in [10] and are listed in Table II. Determining an appropriate value for the range parameter associated with lateral correlation is particularly difficult due to insufficient well data. The 2-D section is assumed to be lithologically varying laterally because of different mineral fractions in CR. We, therefore, take a conservative approach and use

TABLE I

ESTIMATED PARAMETERS IN THE ROCK PHYSICS LIKELIHOOD MODEL. THE ESTIMATED INTERCEPT $\hat{\alpha}$ AND THE SLOPES ($\hat{\beta}_\phi$, $\hat{\beta}_{s_w}$, $\hat{\beta}_{v_c}$) OF POROSITY, WATER SATURATION, AND VOLUME OF CLAY, RESPECTIVELY, ARE DISPLAYED TOGETHER WITH THE ESTIMATED STANDARD DEVIATION $\hat{\sigma}$ FOR EACH REGRESSION MODEL IN THE TOP TABLE. EACH ROW OF THE TABLE CONTAINS THE PARAMETERS ASSOCIATED WITH THE MODEL FOR THE ELASTIC PROPERTY SPECIFIED IN THE LEFTMOST COLUMN. THE ESTIMATED CROSS COVARIANCES BETWEEN THE ELASTIC PROPERTIES, ($\hat{\xi}_{v_p v_s}$, $\hat{\xi}_{v_p \rho}$, $\hat{\xi}_{v_s \rho}$), ARE SHOWN IN THE BOTTOM TABLE

	$\hat{\alpha}$	$\hat{\beta}_\phi$	$\hat{\beta}_{s_w}$	$\hat{\beta}_{v_c}$	$\hat{\sigma}$
$\log(v_p)$	8.528	-1.567	0.085	-0.503	0.034
$\log(v_s)$	8.456	-2.892	0	-0.975	0.066
$\log(\rho)$	1.006	-0.910	0.035	-0.017	0.003

$\hat{\xi}_{v_p v_s}$	$\hat{\xi}_{v_p \rho}$	$\hat{\xi}_{v_s \rho}$
$1.50 \cdot 10^{-3}$	$3.15 \cdot 10^{-5}$	$8.50 \cdot 10^{-5}$

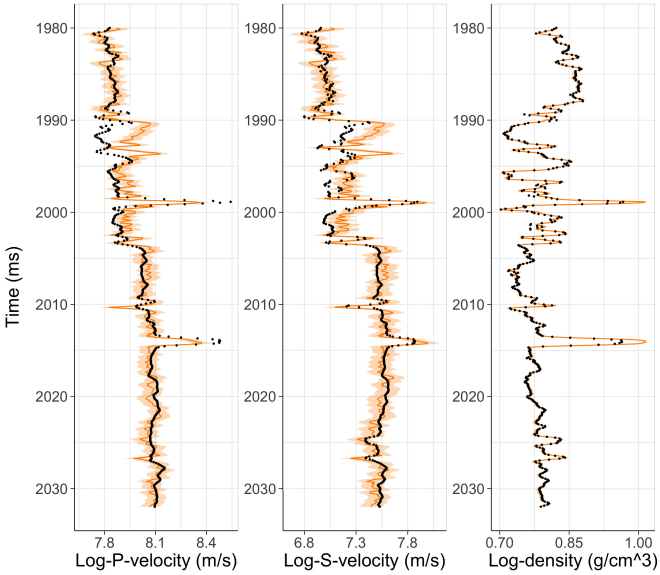

Fig. 6. Predicted and measured logarithmic elastic properties, displayed column-wise from left to right: P-wave velocity, S-wave velocity, and density. The logarithm of the measured elastic properties (points) and of the rock physics predicted elastic properties (orange solid lines) with associated 90% prediction intervals (transparent orange regions) are displayed together.

a degree of lateral correlation that in practice establishes a locationwise lateral dependency that only extends to the two nearest traces in each direction. It is also necessary to specify the anisotropies of porosity and water saturation. Because the 2-D section follows the interpreted horizon of the reservoir, we assume lithological layering to follow the geometry of the section. This lithological layering is described by structural correlation in porosity and volume of shale, represented by $\mathbf{\Omega}_s$, and it is achieved by computing the spatial correlations on a rectangular version of the irregular 2-D section. The fluid content in the reservoir zone is superimposed on the lithology and obeys gravitational effects. Therefore, the correlation structure of water saturation, represented by $\mathbf{\Omega}_h$, is defined to favor

TABLE II

PARAMETER VALUES USED IN THE S-GRF PRIOR MODEL. THE PARAMETERS ASSOCIATED WITH THE BASIS GRF MODEL ARE SHOWN IN THE TOP; THE LOCATIONWISE EXPECTATIONS $\mu_{\tilde{r}_k}$ IN THE LEFTMOST BLOCK, THE LOCATIONWISE VARIANCES $\sigma^2_{\tilde{r}_k}$ IN THE MIDDLE BLOCK, AND THE INTER-VARIABLE CORRELATIONS λ_k TO THE RIGHT, $k = 1, 2, 3$. THE PARAMETERS ASSOCIATED WITH THE AUXILIARY GRF ARE SHOWN IN THE MIDDLE; THE MARGINAL SELECTION SETS A_k TO THE LEFT AND THE CORRELATIONS WITH THE BASIS GRF γ_k TO THE RIGHT. THE RANGE PARAMETERS $\alpha_{k,i}$ ASSOCIATED WITH THE SPATIAL CORRELATION STRUCTURES ARE LISTED IN THE BOTTOM, FOR $k = 1, 2, 3$ AND $i = 1, 2$

$\mu_{\tilde{\phi}}$	0.3	$\sigma^2_{\tilde{\phi}}$	$2.420 \cdot 10^{-3}$	λ_1	-0.25
$\mu_{\tilde{s}_w}$	0.5	$\sigma^2_{\tilde{s}_w}$	$6.561 \cdot 10^{-2}$	λ_2	-0.7
$\mu_{\tilde{v}_c}$	0.15	$\sigma^2_{\tilde{v}_c}$	$2.000 \cdot 10^{-1}$	λ_3	0.5

A_1	$(-\infty, -0]$	γ_1	0.9
A_2	$(-\infty, -1.2] \cup [1.45, \infty)$	γ_2	0.95
A_3	$[-0.15, 0.15] \cup [1.6, 2.2]$	γ_3	0.95

$\alpha_{v,1}$	1	$\alpha_{v,2}$	1	$\alpha_{v,3}$	1
$\alpha_{h,1}$	25	$\alpha_{h,2}$	25	$\alpha_{h,3}$	25

horizontal fluid contacts, which is achieved by computing the spatial correlations on the irregular 2-D section.

The parameter values used in prior model 2 are shown in Table II, except for the lateral correlation that is assigned $\alpha_{h,1} = \alpha_{h,2} = \alpha_{h,3} = 0$, that is, no lateral correlation.

The locationwise prior models for porosity, water saturation, and volume of clay, representing the marginal pdfs in the RF $\mathbf{r}$, are shown in Fig. 7. The prior models are superimposed on histograms of well log data, after outlier removal. The locationwise prior model for porosity is unimodal and notably skewed in sandy regions, whereas the locationwise prior models for water saturation and volume of clay are distinctly bimodal. The distinct bimodality in the prior model for water saturation reflects the gravitational effects assumed to be present, which causes abrupt spatial fluid transitions. Volume of clay has a notable effect on the prior models for porosity and water saturation. We see that the clay effect on the prior model for porosity is a shift of location and an inverse relationship between skewness and volume of clay, whereas the clay effect on the prior model for water saturation is the alteration of the oil and water probabilities, with high volume of clay corresponding to high probability of water.

B. Results

We refer to the posterior models corresponding to prior models 1 and 2 simply as models 1 and 2, respectively. The convergence of the simulation-based model assessments is ensured by running several M-H McMCs from random initial states until the assessed models cannot be distinguished, and by evaluation of locationwise convergence plots [10].

The MMAP predictions from models 1 and 2 are shown in Figs. 8 and 9, respectively. The predictions from model 1 (see Fig. 8) indicate two major high porosity oil zones between the overlying shale layer and the underlying aquifer, separated

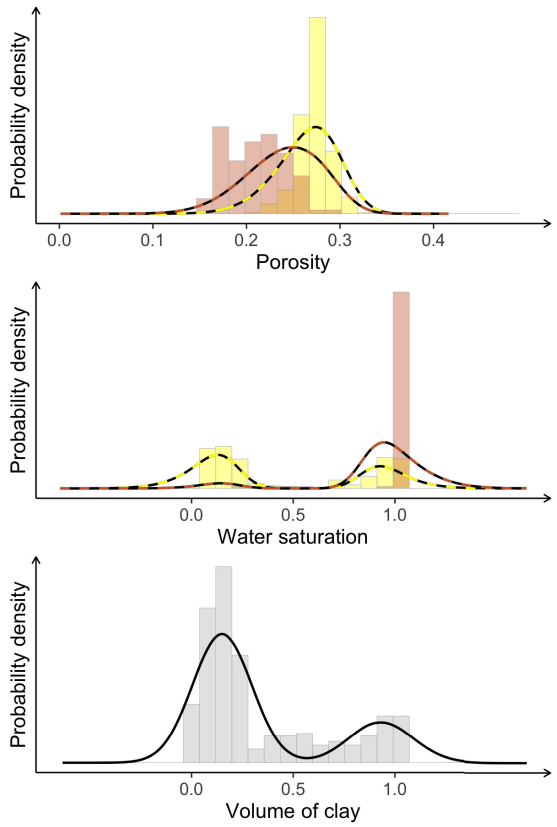

Fig. 7. Locationwise prior models superimposed on histograms of well logs from Well B. The histograms of porosity and water saturation are colored yellow and brown, corresponding to data from sandy and presumably shaly regions, respectively. This classification is based on the bimodal distribution assigned to volume of clay. Moreover, because the prior models for porosity and water saturation are relatively strongly influenced by the volume of clay, a sandy prior model is displayed in hatched yellow and a shaly prior model is displayed in hatched brown. These models are based on the expected clay volume within each clay mode.

by CR where, as suspected, a considerable presence of high clay content is reflected in the predicted volumes of clay. Moreover, the geometry of the predicted oil zones can be seen to have a natural explanation in the predicted volumes of clay. A few specks of low water saturation are predicted outside the major oil zones, but these are most likely reflecting unsupported lithological heterogeneity or noise in the seismic AVO data. The predicted water saturations exhibit strong continuity and smoothness, with distinctly defined regions of low values and high values. The predictions from model 2 (see Fig. 9) indicate high porosity oil zones on each side of CR, between the overlying shale layer and the underlying aquifer. The geometry of the major oil zones appears to have a natural explanation in the predicted volumes of clay. However, the major oil zone to the right of CR is not contained within the 2-D section and appears to continue in the top horizon above CR. Moreover, several minor disconnected regions of low water saturation are predicted in CR, which based on the volume of clay predictions in CR are overlaid by water. Despite a prior model without lateral correlation, the predictions clearly exhibit continuity, indicating strong continuity in the seismic AVO data. Both models predict the top of the reservoir zone to primarily have high water saturation and high clay content, which strongly indicates the presence of an overlying shale layer. The porosity predictions from the two models are very similar, but the predicted water saturations and volumes of clay differ notably in CR. The predictions from model 1 indicate that this region does not contain oil, whereas the predictions from model 2 indicate several irregular and disconnected regions of low water saturation and unphysical fluid transitions. Based on the seismic data in Fig. 4, we do not expect oil in CR. The predicted volumes of clay from model 1 indicate a dominant presence of high clay content in CR, whereas model 2 indicates more of a mix between sandy regions and shaly regions. The volume of clay predictions from model 1 seem geologically more plausible.

The locationwise variances of models 1 and 2 are shown in Figs. 10 and 11, respectively. The variances associated with the porosity predictions from the two models are very similar and relatively low, except for along the top and bottom of the 2-D section and along a thin structure across CR. The variances of water saturation and volume of clay from model 1 (see Fig. 10) display a similar pattern with respect to their corresponding predictions: the variances appear relatively low except for at the borders separating low value and high value regions in the MMAP predictions, and this effect is particularly apparent for water saturation. The relatively strong variance contrast for water saturation is likely due to less mixing of low value and high value regions in the predictions than in the volume of clay predictions, which results in lower background variance. Moreover, the contrast between low and high variance is stronger for water saturation and volume of clay than for porosity because the locationwise posteriors of porosity are unimodal, while they are bimodal at the region borders for water saturation and volume of clay. Finally, the variances appear to be relatively low to the left of CR, coinciding with the strongest signals in the seismic AVO data (see Fig. 4). The variances of water saturation and volume of clay from model 2 (see Fig. 11) appear particularly high in CR and moderately high to the right of CR. To the left of CR, where the strongest signals in the seismic AVO data are, some identifiable regions can be discerned and the background variance appears relatively low. Upon comparison of the two models, the variances of model 1 appear to be more structured and the background variances seem to be lower. This is particularly evident for water saturation. Consequently, predictions from model 2 are more uncertain than predictions from model 1, as expected, because model 1 incorporates data from neighboring traces and thereby reduces uncertainty. The differences in the locationwise variances should generate apparent differences in realizations from the two posterior models and for water saturation in particular.

The inversion results from models 1 and 2 along Well A and Well B are jointly presented in Fig. 12. The two models yield very similar porosity results; the predicted porosity profiles are in good agreement with the well log data and the associated HPDI looks reasonable. The predicted water saturation profiles are mostly in good agreement with the well log data, but a few notable exceptions occur. In Well A, the predictions from the two models along the top reservoir suggest the presence of a

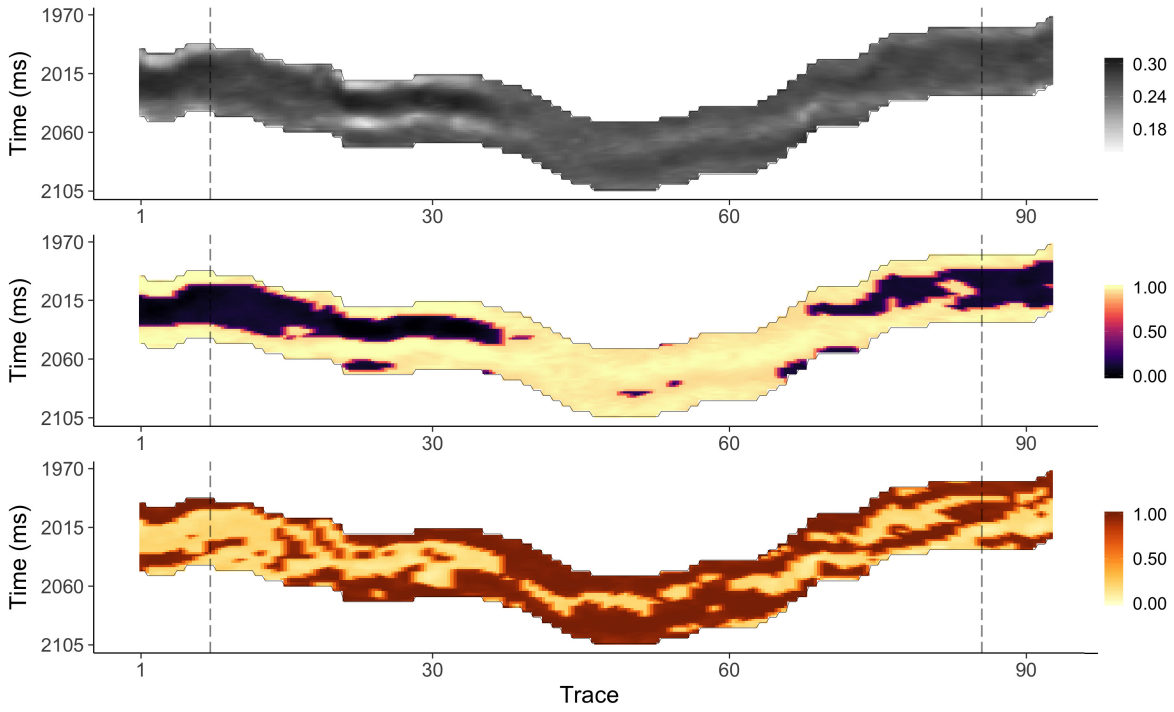

Fig. 8. MMAP predictions from model 1. (Top) Porosity. (Middle) Water saturation. (Bottom) Volume of clay. The locations of Well A and Well B are marked.

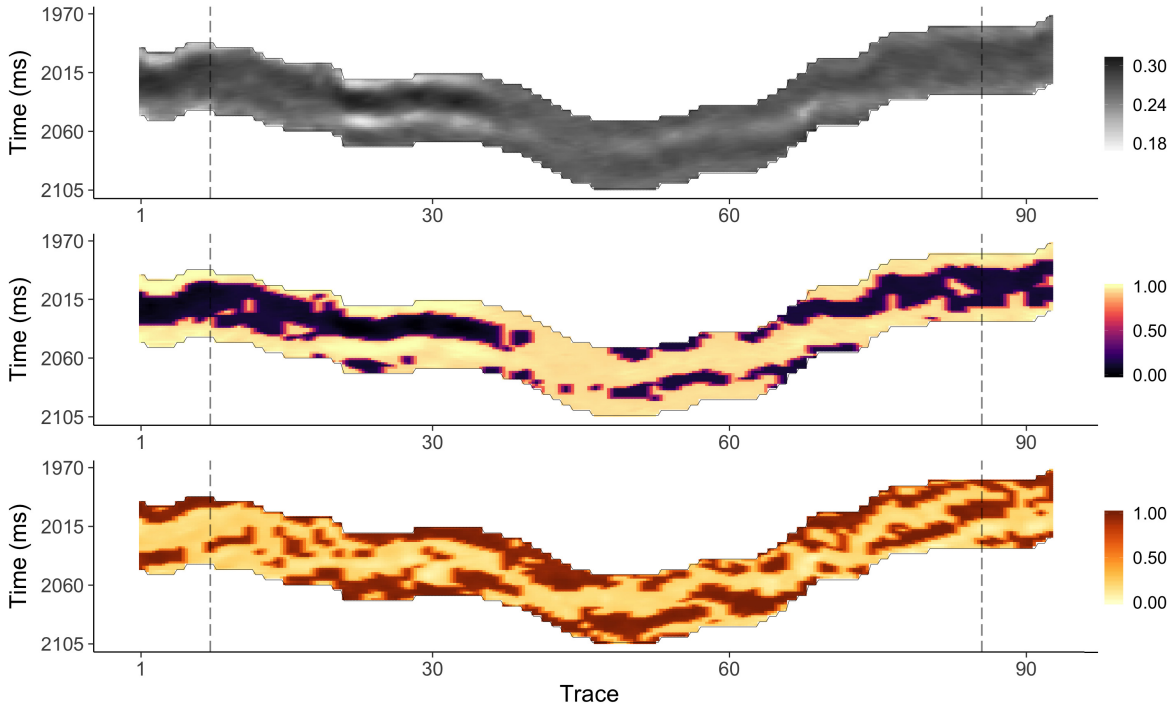

Fig. 9. MMAP predictions from model 2. (Top) Porosity. (Middle) Water saturation. (Bottom) Volume of clay. The locations of Well A and Well B are marked.

shale layer that is not indicated by the well logs. Moreover, the two models predict different OWC locations, with model 1 predicting the OWC location roughly 4 ms deeper than model 2. Because Well A is not located exactly on the cross line under study, it is unclear whether these well log data are representative; hence, we cannot conclude anything about these apparent discrepancies. In Well B, neither model predicts the highly water-saturated interval between 1998 and 2002 ms. However, this high water saturation occurrence is located within the interval in which the rock physics model performs relatively poorly. The predicted volume of clay profiles from models 1 and 2 are mostly in good agreement but differ at

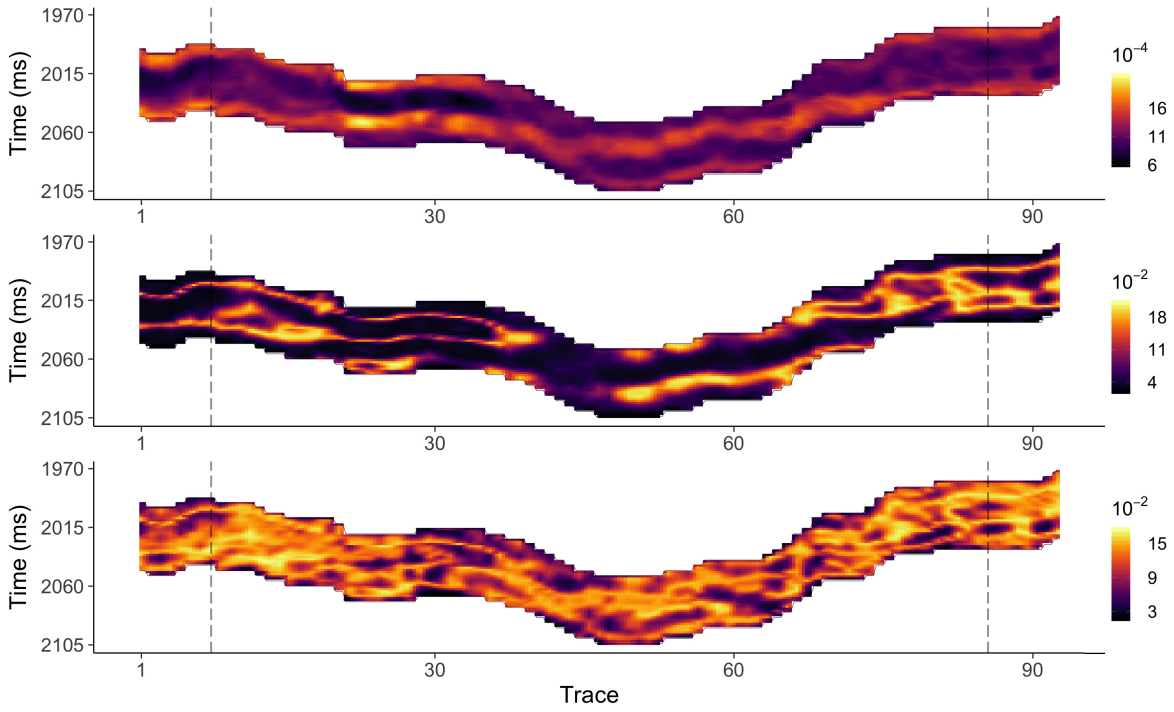

Fig. 10. Locationwise variances of model 1. (Top) Porosity. (Middle) Water saturation. (Bottom) Volume of clay. The locations of Well A and Well B are marked.

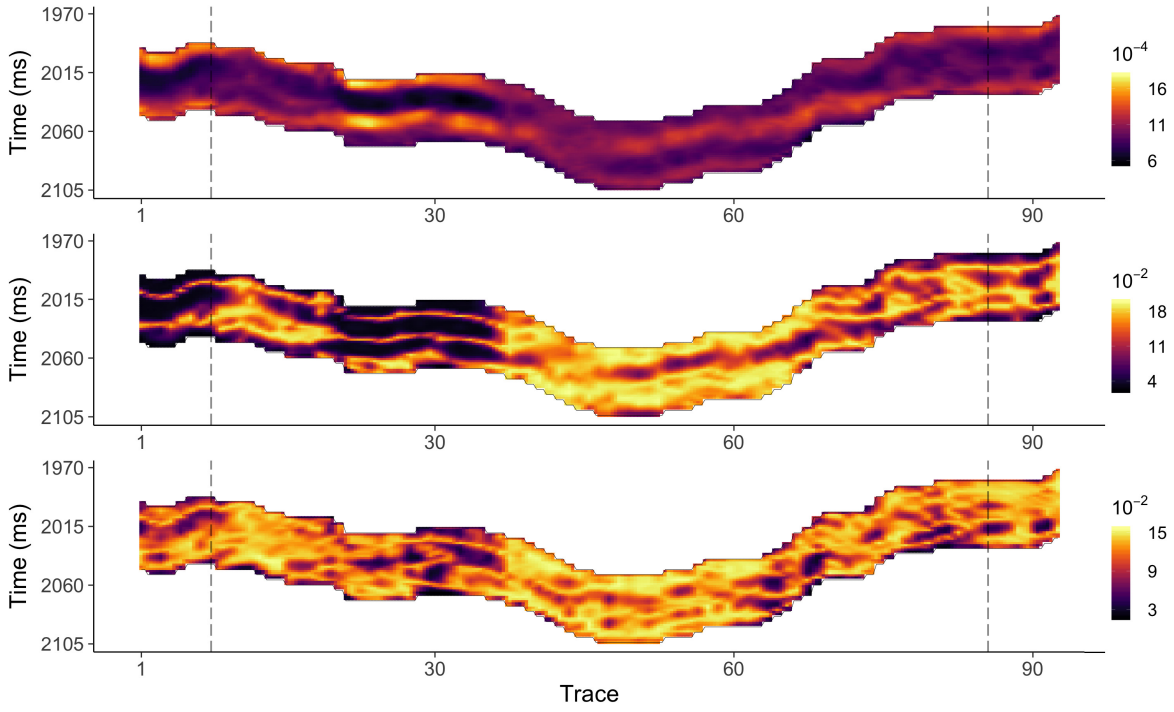

Fig. 11. Locationwise variances of model 2. (Top) Porosity. (Middle) Water saturation. (Bottom) Volume of clay. The locations of Well A and Well B are marked.

several lithological transitions. In Well A, the two models produce very similar volume of clay results, but model 1 predicts the deepest high clay content interval to start higher than what model 2 does. In Figs. 8 and 9, we see that model 1 predicts a connected high clay content layer from the left of the 2-D section and through Well A, whereas model 2 predicts disconnected regions here. A connected region is geologically more likely. In Well B, the two models predict a different thickness of the overlying shale layer. Based on the well log data, model 1 appears to predict the shale layer thickness accurately, whereas model 2 underpredicts. Both models seem to overpredict the thickness of the high clay

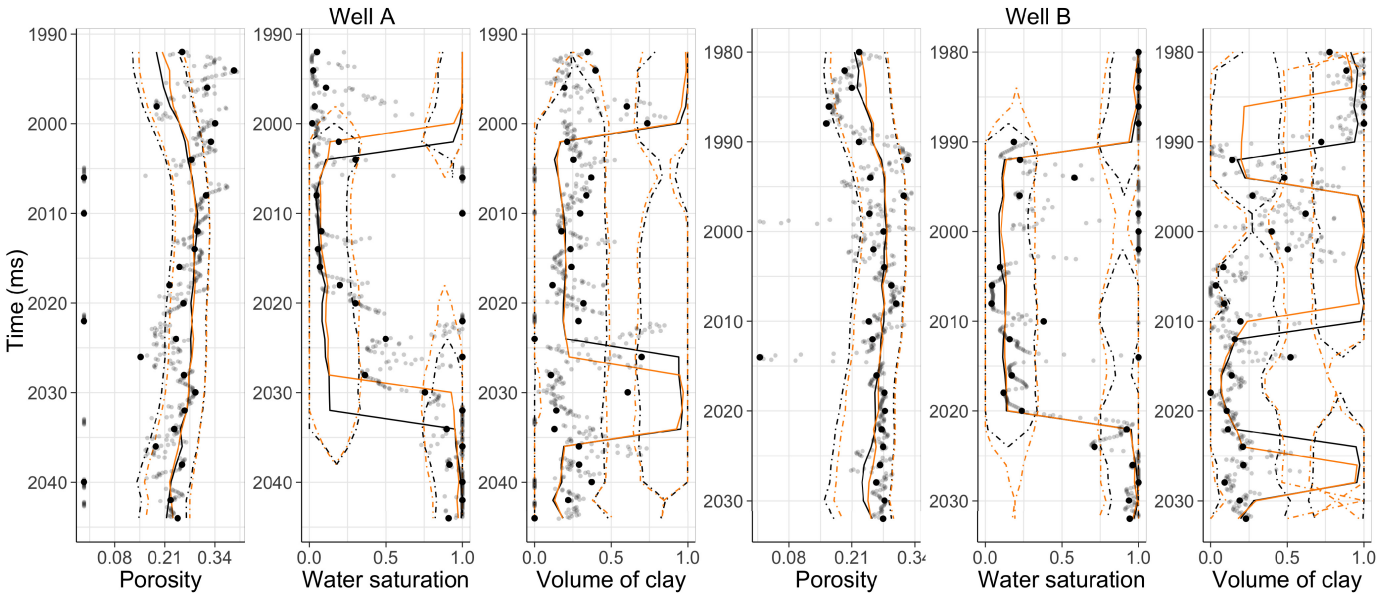

Fig. 12. Inversion results from model 1 (black) and model 2 (orange) along Well A and Well B. The MMAP predictions (solid lines) are displayed with 90% HPDI (dotted-dashed lines). Well log data are displayed on the reservoir grid (black points) and on the well log grid (transparent points).

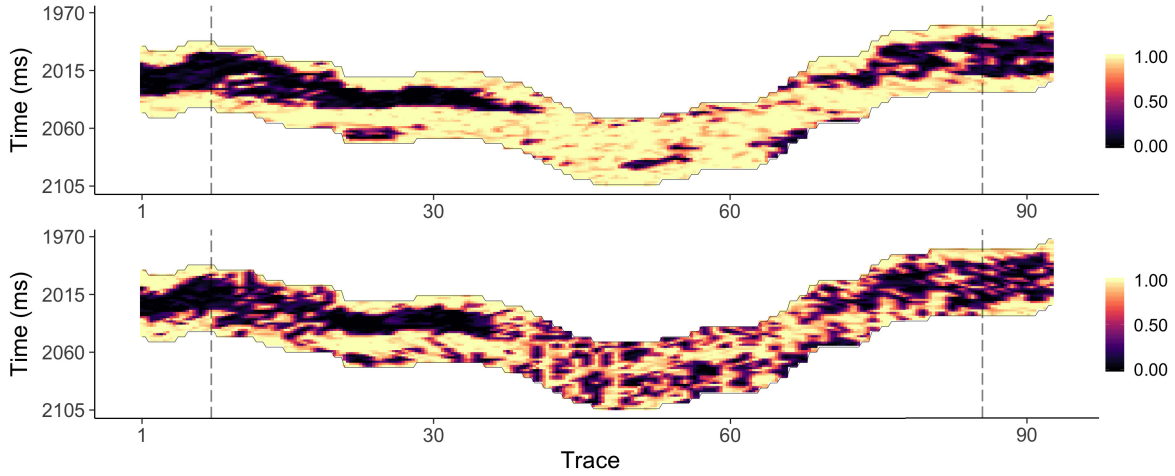

Fig. 13. One realization of water saturation from each model, truncated to [0, 1]. (Top) Model 1. (Bottom) Model 2.

content interval in the middle of the well, but model 2 predicts a slightly shorter interval than model 1. Note that the possibly limestone-influenced interval is located within these predicted high clay content intervals. Finally, model 2 predicts a slightly shorter interval of high clay content than model 1 near the deeper end of the reservoir profile. Here, the predictions from model 2 appear to be more accurate than the predictions from model 1. As expected from the locationwise model variances shown in Figs. 10 and 11, the HPDI from model 2 reflects more bimodality in the locationwise posteriors of water saturation than the HPDI from model 1.

One realization of water saturation from each model, truncated to the physical range $[0, 1]$, is shown in Fig. 13. These realizations should be compared with the corresponding MMAP predictions in Figs. 8 and 9. The realization from model 1 exhibits most features of the MMAP prediction, with identifiable regions of low water saturation and with CR being a region of mostly high water saturation. In CR and to the right of CR, the realization appears more heterogeneous than the MMAP, as expected based on the locationwise posterior variances shown in Fig. 10. The realization from model 2 appears similar to the corresponding MMAP prediction to the left of CR, but it is otherwise difficult to recognize features of the MMAP due to very high heterogeneity. The large locationwise posterior variances in Fig. 11 support this predominant heterogeneity and lack of spatial structure. Realizations of porosity and volume of clay do not have as marked differences, but the clear differences observed in the water saturation realizations may still impact potential subsequent results, such as production forecasting by fluid flow simulation.

Quantitative performance measures, based on well log data on the reservoir grid, are presented for the inversion results along Well A and Well B in Tables III and IV, for models 1

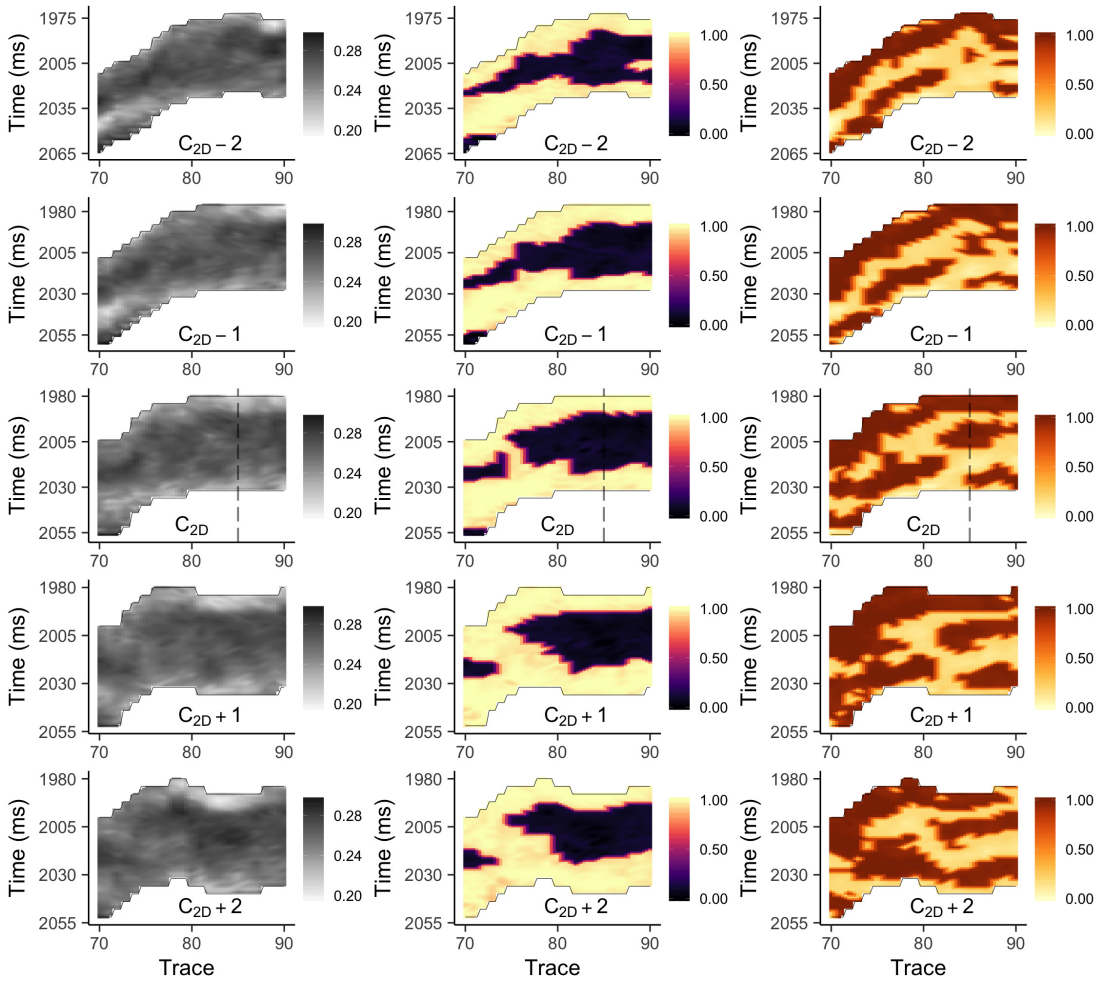

Fig. 14. MMAP predictions, displayed row-wise from top to bottom for crosslines $C_{2\text{-D}-2}$ to $C_{2\text{-D}+2}$. (Left column) Porosity. (Middle column) Water saturation. (Right column) Volume of clay. The location of Well B is marked.

TABLE III
RMSE AND EC OF THE 90% HPDI ALONG WELLS A AND B FOR MODEL 1

	Model 1			
	Well A		Well B	
	RMSE	EC	RMSE	EC
$\hat{\phi}$	0.121	0.630	0.059	0.852
$\hat{\mathbf{s}}_w$	0.606	0.519	0.397	0.741
$\hat{\mathbf{v}}_c$	0.392	0.852	0.492	0.741

TABLE IV
RMSE AND EC OF THE 90% HPDI ALONG WELLS A AND B FOR MODEL 2

	Model 2			
	Well A		Well B	
	RMSE	EC	RMSE	EC
$\hat{\phi}$	0.118	0.630	0.059	0.852
$\hat{\mathbf{s}}_w$	0.545	0.630	0.390	0.778
$\hat{\mathbf{v}}_c$	0.394	0.889	0.495	0.815

and 2 respectively. As expected, the RMSE and EC indicate that the results in Well B are overall better than in Well A. The difference in result quality between the two wells is mostly a consequence of the conflicting predictions and observations at the top of Well A. The two models perform very similarly in terms of RMSE. Neither model achieves the desired EC of 0.9, which is most likely a result of partly unrepresentative data in Well A and a few poorly supported data points in Well B. Model 1 appears to have lower EC than model 2, as expected, due to variance reduction from lateral correlation. The most favorable feature of the predictions from model 1 is the relatively high homogeneity compared to the predictions from model 2 (see Figs. 8 and 9), which strongly suggests that the lateral coupling in model 1 reduces the effects of trace-unique signal errors in the seismic AVO data.

V. CASE: REAL SEISMIC AVO DATA FROM A 3-D VOLUME

We apply the proposed seismic inversion methodology to a 3-D volume of the Kneler field in the Alvheim oil and gas field, in the North Sea. The 3-D volume consists of five crosslines containing traces 70–90; hence, the region between traces 70 and 90 of the 2-D section studied previously, see Fig. 1, is contained. The center crossline in the 3-D volume is referred to as $C_{2\text{-D}}$, which is the crossline studied in Section IV. The 3-D volume contains a total of 105 traces with a regular inter-trace spacing of 50 m, each of which covers a

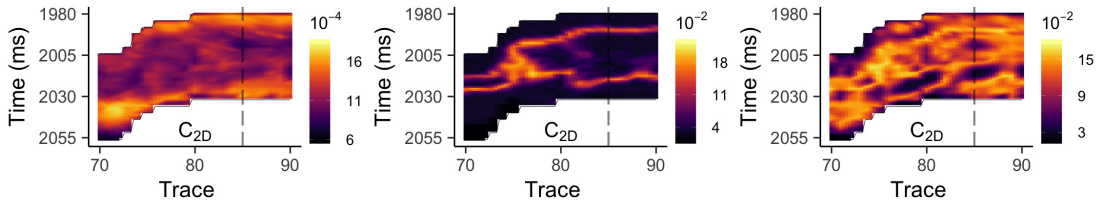

Fig. 15. Locationwise variances of the posterior on C_{2-D}. (Left) Porosity. (Middle) Water saturation. (Right) Volume of clay. The location of Well B is marked.

depth range of 52 ms in two-way time, that is, the distance between inlines and crosslines is 50 m.

The reservoir grid $\mathcal{G}_r$ consists of $n_r = 2835$ grid points that are regularly spaced laterally and with trace-unique vertical gridding, whereas the seismic grid $\mathcal{G}_d$ consists of $n_d = 1470$ grid points with similar grid structure. The trace-unique vertical gridding consists of 27 points in the reservoir grid and 14 points in the seismic grid.

A. Model Construction

The model construction is based on Well B; hence, the likelihood model is, except for dimensionality, identical to the likelihood model used in Section IV with estimated wavelet shown in Fig. 5 and rock physics parameters listed in Table I. Moreover, the prior model parameter values are also identical and are shown in Table II. However, note that the prior model is laterally correlated in one additional spatial dimension compared to the laterally correlated prior model used in Section IV.

B. Results

The MMAP predictions are shown in Fig. 14. The MMAP predictions in Section IV should be compared to the predictions on crossline $C_{2\text{-D}}$, which appear very similar. However, a notable exception can be seen in the water saturations and volumes of clay: the oil region and the high clay content region in the middle are now apparently disconnected. The geometry of the oil zone and the high clay content regions slowly varies across crosslines, demonstrating lateral continuity perpendicular to the 2-D studied in Section IV.

The locationwise variances of the posterior model on crossline $C_{2\text{-D}}$ are shown in Fig. 15. Compared to the locationwise variances of the posterior models in Section IV, shown in Figs. 10 and 11, the variances appear to be reduced. This is particularly evident in the variances of water saturation, which now have more structure due to the disappearance of some high variance borders inside the oil zone. The variance reduction is expected due to conditioning on additional neighboring traces perpendicular to the orientation of the 2-D section studied in section IV in the sampling. Consequently, realizations from this posterior model should exhibit less heterogeneity than realizations from either of the posterior models in the previous section.

The inversion result is presented along Well B in Fig. 16. The MMAP predictions are overall in good agreement with the observations for all reservoir properties. Furthermore, the HPDI appears reasonable. Compared to the inversion

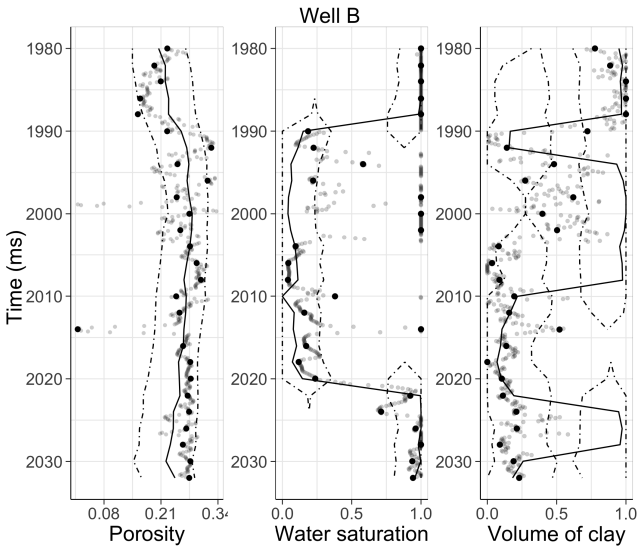

Fig. 16. Inversion result along Well B. The MMAP predictions (solid lines) with 90% HPDI (dotted-dashed lines). Well log data are displayed on the reservoir grid (black points) and the well log grid (transparent points).

TABLE V
RMSE AND EC OF THE 90% HPDI ALONG WELL B

	RMSE	EC
$\hat{\phi}$	0.057	0.852
$\hat{\mathbf{s}}_w$	0.392	0.741
$\hat{\mathbf{v}}_c$	0.483	0.741

results along Well B in Section IV, the porosity result appears as very similar. The predicted water saturation profile is very similar to the previously predicted profiles, but the associated HPDI now reflects less bimodality in the locationwise posteriors. Finally, the predicted volume of clay profile is consistent with the predicted volume of clay profile from the laterally correlated model in Section IV but does not overpredict the thickness of the high clay content interval in the middle of the well as much. Moreover, the associated HPDI reflects less bimodality in the locationwise posteriors.

Quantitative performance measures, based on well log data on the reservoir grid, are presented for the inversion results along Well B in Table V. Compared to the RMSE and EC of model 1 along Well B in Section IV, the RMSE has slightly improved for all reservoir properties. The ECs have not changed.

VI. CONCLUSION

A Bayesian seismic AVO inversion scheme for porosity, water saturation, and volume of clay is proposed. The prior

model is a laterally correlated S-GRF, which can represent the gravitationally induced bimodality observed in the water saturations. The likelihood model is Gauss-linear, for which the S-GRF prior model is conjugate; hence, the posterior model is also an S-GRF. An alternative S-GRF prior model without lateral correlation is defined for comparison through seismic inversion of a 2-D section of real seismic AVO data from the Kneler field in the Alvheim oil and gas field in the North Sea. Two major high porosity oil zones are identifiable in the inversion results from both models, indicating high lateral continuity in the seismic AVO data. However, the laterally correlated S-GRF provides predictions that are more homogeneous and with more clearly defined regions than the laterally uncorrelated S-GRF. Furthermore, a relative reduction in the locationwise variances is observed in the laterally correlated S-GRF posterior model for water saturation and volume of clay, and this is reflected in realizations of water saturation from the posterior models. Inversion of a 3-D volume containing a region of the 2-D section is performed, and the inversion of the 2-D region is compared between the 2-D and 3-D model. An improvement in the predictions and a reduction in the inversion uncertainty are observed in the 3-D inversion. Hence, although the seismic AVO data appear to have strong lateral continuity, lateral correlation in the prior model for the reservoir properties appears to be favorable, even in conservative amounts as in this study.

Computationally, a laterally uncorrelated prior model is preferable because sampling from the posterior model can be done on a trace-by-trace basis. A laterally correlated prior model entails the involvement of neighboring traces in conditional sampling from the posterior. This requires more complex sampling schemes and higher computer demands. However, conditioning on neighboring traces appears to improve the inversion results and make the results less susceptible to trace-unique signal errors. The laterally correlated S-GRF is a more complex prior model, but the benefits discussed above seem to justify the additional cost this entails.

Appendix
Sampling From an m-Dimensional S-GRF

To draw samples from the m-dimensional and n-variate S-GRF $\mathbf{x}$, we make use of the decomposition

$$\begin{aligned} p(\mathbf{x}) &= p(\tilde{\mathbf{x}}|\boldsymbol{\nu} \in \mathbf{A}) = p(\tilde{\mathbf{x}}|\boldsymbol{\nu})p(\boldsymbol{\nu}|\boldsymbol{\nu} \in \mathbf{A}) \\ &= \varphi_n\left(\tilde{\mathbf{x}};\, \boldsymbol{\mu}_{\tilde{x}|\nu}, \boldsymbol{\Sigma}_{\tilde{x}|\nu}\right) \times \frac{I(\boldsymbol{\nu} \in \mathbf{A})\varphi_n\left(\boldsymbol{\nu};\, \boldsymbol{\mu}_{\nu}, \boldsymbol{\Sigma}_{\nu}\right)}{\int_{\mathbb{R}^n} I(\boldsymbol{\nu} \in \mathbf{A})\varphi_n\left(\boldsymbol{\nu};\, \boldsymbol{\mu}_{\nu}, \boldsymbol{\Sigma}_{\nu}\right)\, \mathrm{d}\boldsymbol{\nu}}. \end{aligned} \tag{A-1}$$

A sample is drawn by first sampling $[\boldsymbol{\nu}|\boldsymbol{\nu} \in \mathbf{A}]$, followed by sampling $\mathbf{x}$ from $\varphi_n(\tilde{\mathbf{x}};\, \boldsymbol{\mu}_{\tilde{x}|\nu}, \boldsymbol{\Sigma}_{\tilde{x}|\nu})$. The S-GRF is assumed to consist of $n = n_v \times n_h$ grid points, with n_v and n_h being the number of grid points vertically and laterally, respectively.

We use the proposal distribution

$$q(\boldsymbol{\nu}_{b|b^n}) = \prod_{i \in b} I(\nu_i \in A)\frac{\varphi_1\left(\nu_i;\, \mu_{\nu_i|\nu_{b^{v,n}}}, \sigma^2_{\nu_i|\nu_{b^{v,n}}}\right)}{\Phi_1\left(A;\, \mu_{\nu_i|\nu_{b^{v,n}}}, \sigma^2_{\nu_i|\nu_{b^{v,n}}}\right)} \tag{A-2}$$

with subindex b^n denoting the set of indices in the neighborhood of block $\mathbf{b}$ and subindex $b^{v,n}$ denoting the union of the set of indices in $\mathbf{b}$ already visited and the block neighborhood. The associated M-H acceptance probability, α, is

$$\begin{aligned} \alpha &= \min\left\{1, \frac{p\left(\boldsymbol{\nu}'_{b|b^n}\right)}{p\left(\boldsymbol{\nu}_{b|b^n}\right)} \cdot \frac{q\left(\boldsymbol{\nu}_{b|b^n}\right)}{q\left(\boldsymbol{\nu}'_{b|b^n}\right)}\right\} \\ &= \min\left\{1, \prod_{i \in b} \frac{\Phi_1\left(A;\, \mu'_{\nu_i|\nu_{b^{v,n}}}, \sigma^2_{\nu_i|\nu_{b^{v,n}}}\right)}{\Phi_1\left(A;\, \mu_{\nu_i|\nu_{b^{v,n}}}, \sigma^2_{\nu_i|\nu_{b^{v,n}}}\right)}\right\}. \end{aligned} \tag{A-3}$$

The blocks and the order in which they are visited are predetermined, and the associated covariance matrices are precomputed to reduce the computational time.

Algorithm 1 Draw k Samples From $\mathbf{x}$ by M-H McMC, Trace-by-Trace

Partition $\tilde{\mathbf{x}}$ and $\boldsymbol{\nu}$ into traces, i.e., $\tilde{\mathbf{x}} \in \mathbb{R}^{n_v}$ and $\boldsymbol{\nu} \in \mathbb{R}^{n_v}$.
Partition each trace into n_b vertical blocks $\mathbf{b}_i \subset \{1, \ldots, n_v\}; i = 1, \ldots, n_b$, and define block neighborhoods $\mathbf{b}_i^n = \{1, \ldots, n_v\} \backslash \mathbf{b}_i$.
Iterate n_h **times**
  Initialize $\boldsymbol{\nu}$ with a value in $\mathbf{A}$.
  Iterate k **times**
    Iterate n_b **times**
      Select vertical block $\mathbf{b}_i$.
      Sample $\boldsymbol{\nu}'_{b_i|b_i^n}$ sequentially from $q(\boldsymbol{\nu}'_{b_i|b_i^n})$.
      Accept $\boldsymbol{\nu} = [\boldsymbol{\nu}'_{b_i|b_i^n}, \boldsymbol{\nu}_{b_i^n}]$ with probability α.
    End
    Sample $\mathbf{x} \sim \varphi_{n_v}(\tilde{\mathbf{x}};\, \boldsymbol{\mu}_{\tilde{x}|\nu}, \boldsymbol{\Sigma}_{\tilde{x}|\nu})$.
  End
End

Algorithm 2 Draw k Samples From $\mathbf{x}$ by M-H McMC

Partition the field into n_b m-dimensional rectangular blocks, $\mathbf{b}_i \subset \{1, \ldots, n\}; i = 1, \ldots, n_b$, and define block neighborhoods $\mathbf{b}_i^n \subseteq \mathbf{b}_i^c$, with $\mathbf{b}_i^c = \{1, \ldots, n\} \backslash \mathbf{b}_i$ being the block complements. The spatial correlation in the field will influence the extent of the neighborhoods.
Initialize $\boldsymbol{\nu}$ with a value in $\mathbf{A}$.
Iterate k **times**
  Iterate n_b **times**
    Select block $\mathbf{b}_i$.
    Sample $\boldsymbol{\nu}'_{b_i|b_i^n}$ sequentially from $q(\boldsymbol{\nu}'_{b_i|b_i^n})$.
    Accept $\boldsymbol{\nu} = [\boldsymbol{\nu}'_{b_i|b_i^n}, \boldsymbol{\nu}_{b_i^c}]$ with probability α.
  End
  Sample $\mathbf{x} \sim \varphi_n(\tilde{\mathbf{x}};\, \boldsymbol{\mu}_{\tilde{x}|\nu}, \boldsymbol{\Sigma}_{\tilde{x}|\nu})$.
End

Acknowledgment

This research is part of the Uncertainty in Reservoir Evaluation (URE) activity at the Norwegian University of Science and Technology (NTNU), Trondheim, Norway. The authors would like to thank Aker BP, Trondheim, for data access and the right to publish. The authors acknowledge the application of the R-packages MASS and akima in the computational algorithms and data visualization.

REFERENCES

[1] K. Aki and P. G. Richards, *Quantitative Seismology: Theory and Methods*. New York, NY, USA: W.H. Freeman and Co, 1980.

[2] D. Allard and P. Naveau, "A new spatial skew-normal random field model," *Commun. Statist. Theory Methods*, vol. 36, no. 9, pp. 1821–1834, Jul. 2007.

[3] R. B. Arellano-Valle, M. D. Branco, and M. G. Genton, "A unified view on skewed distributions arising from selections," *Can. J. Statist.*, vol. 34, no. 4, pp. 581–601, Dec. 2006.

[4] S. Brooks, A. Gelman, G. Jones, and X.-L. Meng, *Handbook of Markov Chain Monte Carlo*. London, U.K.: Chapman & Hall, 2011.

[5] A. Buland and H. Omre, "Bayesian linearized AVO inversion," *Geophysics*, vol. 68, no. 1, pp. 185–198, Jan. 2003.

[6] A. Buland, O. Kolbjørnsen, and H. Omre, "Rapid spatially coupled AVO inversion in the Fourier domain," *Geophysics*, vol. 68, no. 3, pp. 824–836, May 2003.

[7] L. P. de Figueiredo, D. Grana, F. L. Bordignon, M. Santos, M. Roisenberg, and B. B. Rodrigues, "Joint Bayesian inversion based on rock-physics prior modeling for the estimation of spatially correlated reservoir properties," *Geophysics*, vol. 83, no. 5, pp. M49–M61, Sep. 2018.

[8] J. Eidsvik, P. Avseth, H. Omre, T. Mukerji, and G. Mavko, "Stochastic reservoir characterization using prestack seismic data," *Geophysics*, vol. 69, no. 4, pp. 978–993, Jul. 2004.

[9] T. Fjeldstad and D. Grana, "Joint probabilistic petrophysics-seismic inversion based on Gaussian mixture and Markov chain prior models," *Geophysics*, vol. 83, no. 1, pp. R31–R42, Jan. 2018.

[10] O. B. Forberg, Ø. Kjøsnes, and H. Omre, "Bayesian seismic amplitude variation with offset inversion for reservoir variables with bimodal spatial histograms," *Geophysics*, vol. 86, no. 3, pp. R331–R350, May 2021.

[11] O. B. Forberg, D. Grana, and H. Omre, "Bayesian inversion of time-lapse seismic AVO data for multimodal reservoir properties," *IEEE Trans. Geosci. Remote Sens.*, early access, Jan. 20, 2021, doi: 10.1109/TGRS.2020.3046102.

[12] D. Grana and E. Della Rossa, "Probabilistic petrophysical-properties estimation integrating statistical rock physics with seismic inversion," *Geophysics*, vol. 75, no. 3, pp. 21–37, May 2010.

[13] D. Grana, T. Fjeldstad, and H. Omre, "Bayesian Gaussian mixture linear inversion for geophysical inverse problems," *Math. Geosci.*, vol. 49, no. 4, pp. 493–515, May 2017.

[14] J. Gunning and M. E. Glinsky, "Delivery: An open-source model-based Bayesian seismic inversion program," *Comput. Geosci.*, vol. 30, no. 6, pp. 619–636, Jul. 2004.

[15] V. Hasselblad, "Estimation of parameters for a mixture of normal distributions," *Technometrics*, vol. 8, no. 3, pp. 431–444, Aug. 1966.

[16] O. Karimi, H. Omre, and M. Mohammadzadeh, "Bayesian closed-skew Gaussian inversion of seismic AVO data for elastic material properties," *Geophysics*, vol. 75, no. 1, pp. R1–R11, Jan. 2010.

[17] M. Landrø, "Discrimination between pressure and fluid saturation changes from time-lapse seismic data," *Geophysics*, vol. 66, no. 3, pp. 836–844, 2001.

[18] A. L. Larsen, M. Ulvmoen, H. Omre, and A. Buland, "Bayesian lithology/fluid prediction and simulation on the basis of a Markov-chain prior model," *Geophysics*, vol. 71, no. 5, pp. R69–R78, Sep. 2006.

[19] G. Mavko, T. Mukerji, and J. Dvorkin, *The Rock Physics Handbook*. Cambridge, U.K.: Cambridge Univ. Press, 2009.

[20] K. Mosegaard and A. Tarantola, "Monte Carlo sampling of solutions to inverse problems," *J. Geophys. Res., Solid Earth*, vol. 100, no. B7, pp. 12431–12447, Jul. 1995.

[21] H. Omre and K. Rimstad, "Bayesian spatial inversion and conjugate selection Gaussian prior models," *SIAM/ASA J. Uncertainty Quantification*, vol. 9, no. 2, pp. 420–445, Jan. 2021.

[22] A. Ray, D. L. Alumbaugh, G. M. Hoversten, and K. Key, "Robust and accelerated Bayesian inversion of marine controlled-source electromagnetic data using parallel tempering," *Geophysics*, vol. 78, no. 6, pp. E271–E280, Nov. 2013.

[23] K. Rimstad and H. Omre, "Skew-Gaussian random fields," *Spatial Statist.*, vol. 10, pp. 43–62, Nov. 2014.

[24] K. Rimstad, P. Avseth, and H. Omre, "Hierarchical Bayesian lithology/fluid prediction: A north sea case study," *Geophysics*, vol. 77, no. 2, pp. B69–B85, Mar. 2012.

[25] M. K. Sen and P. L. Stoffa, "Bayesian inference, Gibbs' sampler and uncertainty estimation in geophysical inversion," *Geophys. Prospecting*, vol. 44, no. 2, pp. 313–350, 1996.

[26] A. Tarantola, *Inverse Problem Theory and Methods for Model Parameter Estimation*. Philadelphia, PA, USA: SIAM, 2005.

[27] Y. Wang, *Seismic Inversion: Theory and Applications*. Hoboken, NJ, USA: Wiley, 2006.

[28] K. B. Zoeppritz, "Vllb. On reflection and transmission of seismic waves by surfaces of discontinuity," in *Nachrichten von der Königlichen Gesellschaft der Wissenschaften Zu Göttingen*. Mathematisch-Physikalische Klasse, 1919, pp. 66–84.

Ole Bernhard Forberg received the M.Sc. degree in industrial mathematics from the Norwegian University of Science and Technology (NTNU), Trondheim, Norway, in 2017, where he is currently pursuing the Ph.D. degree in statistics with the Department of Mathematical Sciences.

He joined the "Uncertainty in Reservoir Evaluation" (URE) research initiative at NTNU in 2017. His main research interests include Bayesian inversion and computationally intensive statistical methods, with a particular interest in spatiotemporal statistics, seismic inversion, and selection Gaussian random fields.

Øyvind Kjøsnes received the M.Sc. degree in applied reservoir geophysics from the University of Bergen, Bergen, Norway, in 2007.

He has worked in the oil and gas industry since 2007 and specializes in seismic reservoir characterization. He is currently the Lead Geophysicist of Aker BP, Trondheim, Norway. His main research and development focus is on quantitative geophysics methods, through development and application of a broad range of seismic processing and conditioning methodologies, and analysis by Bayesian seismic inversion and machine learning techniques.

Mr. Kjøsnes is the Co-Chairman of the Annual EAGE Seismic Inversion Conference.

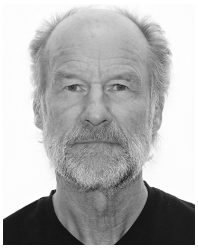

Henning Omre received the M.Sc. degree in statistics from the Norwegian University of Science and Technology (NTNU), Trondheim, Norway, in 1975, and the Ph.D. degree in geostatistics from Stanford University, Stanford, CA, USA, in 1985.

He has worked with the Norwegian Computing Center, Oslo, Norway, from 1976 to 1992. He joined NTNU as a Professor in 1992. From 1994 to 2019, he was the Head of the research initiative "Uncertainty in Reservoir Evaluation" (URE). He is currently a Professor of statistics with the Department of Mathematical Sciences, NTNU. His main research interests include spatiotemporal statistics and Bayesian inversion.